Applied Ocean Research 175 (2026) 105206

Contents lists available at ScienceDirect

Applied Ocean Research

journal homepage: www.elsevier.com/locate/apor

Research paper

A lattice Boltzmann method for floating oscillating water column WECs

Baoming Guo [a], Dezhi Ning [b], Jianping Meng [c], Qianze Zhuang [b], Zhihua Xie [a,*], Shunqi Pan [a,*]

[a] Hydro-environmental Research Centre, School of Engineering, Cardiff University, CF24 3AA, UK
[b] State Key Laboratory of Coastal and Offshore Engineering, Dalian University of Technology, Dalian 116024, China
[c] Research IT, IT Services, University of Liverpool, L69 3GG, UK

ARTICLE INFO

Keywords:
Lattice Boltzmann method (LBM)
Potential-flow model
Floating OWC
Hydrodynamic efficiency

ABSTRACT

In this study, a hierarchical multi-fidelity modelling framework, combining the lattice Boltzmann method (LBM) and potential-flow approach, is developed to investigate the two-dimensional floating oscillating water column (OWC) wave energy converters (WEC). The framework is built on a potential-flow model using the matching eigenfunction expansions, enabling efficient parametric screening and preliminary optimization, and then refined through viscous-flow LBM simulations to obtain more physically realistic estimations of hydrodynamic efficiency and motion responses. Numerically, this LBM based modelling framework incorporates a single-phase volume-of-fluid (VOF) method for capturing air-water interface and employs an interpolated bounce back-Galilean-invariant momentum exchange method (IBB-GIMEM) for handling air-water-solid interactions. Wave generation and absorption are realized through a momentum source technique and a perfectly matched layer (PML), respectively. Furthermore, a pneumatic model accounting for air compressibility is two-way coupled with this hydrodynamic model to evaluate the pressure response within the OWC chamber. Validation against experimental measurements confirms that the proposed modelling framework reliably captures both the hydrodynamic motions and the pneumatic dynamics. This framework is subsequently utilized to study the power extraction performance of an elastically constrained heave-only OWC WEC. Results highlight the effectiveness of this staged modelling strategy in providing a computationally efficient yet physically detailed analysis of floating OWC-wave interactions, supporting its application in the design and optimization of wave energy systems.

1. Introduction

An oscillating water column (OWC) wave energy converter (WEC) is widely recognized as one of the most promising technologies for harnessing ocean energy, owing to the simple mechanical design and operational principle (Falcão and Henriques, 2016). The OWC consists of a hollow structure and an air turbine positioned at the top. Induced by the external waves, air trapped above the water surface within the OWC chamber flows through the self-rectifying turbine, propelling its rotation to generate electricity. Numerous technologies related to OWC have been proposed and studied (Falcão and Henriques, 2016; Doyle and Aggidis, 2019; Portillo et al., 2020; Zhou et al., 2023) and a few prototypes have been operating under real ocean conditions, rated 100 Kw to 1 Mw (Falcão and Henriques, 2016). Despite extensive research and development, some crucial issues still exist in the performance studies of OWCs, noticeably in the following two aspects: (i) It is of practical significance to investigate floating OWCs for the broader exploration space and higher energy flux density in open sea. However, this raises new technological challenges such as addressing mooring systems and device motions (Wang et al., 2022); and (ii) Validated against physical experiments (Elhanafi et al., 2017; Wang et al., 2018), the computational fluid dynamics (CFD) methods (Crespo et al., 2017; Luo et al., 2014; Opoku et al., 2023; Wang et al., 2023) have been increasingly employed to study the power extraction characteristics of OWCs, offering the capability of simulating the real fluid effects (i.e., vortex and strong nonlinearity) and more realistic predictions. However, the high computational cost of CFD solvers limits their applicability to the OWC-wave interaction that involves complex air-water interface capturing and coupled air-water-solid interactions.

The wave interactions with onshore OWC WECs have been extensively investigated through experimental, analytical, and numerical methods. Among these, CFD models are considered as feasible

* Corresponding authors.
E-mail addresses: zxie@cardiff.ac.uk (Z. Xie), pans2@cardiff.ac.uk (S. Pan).

https://doi.org/10.1016/j.apor.2026.105206
Received 1 December 2025; Received in revised form 25 June 2026; Accepted 4 August 2026
Available online 22 August 2026

alternatives to physical experiments, and various solvers have been developed based on the Navier-Stokes (NS) equation (Opoku et al., 2023). For example, Vyzikas et al. (2017) developed a two-dimensional (2D) k-ε Reynolds-Averaged Navier-Stokes (RANS) -VOF model in OpenFOAM to study the performance of an OWC with or without Power Take-off (PTO) system. The visual velocity fields for two phases offers solid evidence that the bottom opening dominates the flow pattern at the vicinity and the high-speed jet-type airflow induces a significant amount of turbulence. Simonetti et al. (2018) built a compressible multiphase solver using Large Eddy Simulation-VOF model, examining the effect of the air compressibility on capture width ratio (CWR). Additionally, a WEC array can contribute constructive impacts on the power extraction. In Ref. (Wang et al., 2023), a three-unit cylindrical OWC with various arrangements were compared through a k-ω Shear Stress Transport (SST) RANS-VOF model. Recent research has also focused on offshore floating OWCs due to their independence from submarine topography and their ability to exploit more energetic wave resources. Luo et al. (2014) utilized a 2D numerical wave tank (NWT) in the commercial software Fluent to study the hydrodynamics of a heave-only floating OWC. It was found that the heave motion induces an additional local maximum on hydrodynamic efficiency and broadens the effective bandwidth, while the peak efficiency decreases. Mia et al. (2023) investigated an elastically supported heave-only OWC WEC by a 2D numerical model based on an arbitrary Lagrangian-Eulerian scheme and the Petrov-Galerkin finite element method. Additionally, a k-ε RANS-VOF model was developed in CFD package Star-CCM+ to explore the hydrodynamic behaviours of an OWC integrated into a heaving breakwater (Fu and Cheng, 2023). This hybrid WEC-breakwater system demonstrated enhanced wave attenuation, albeit with a reduction in power extraction efficiency. Elhanafi et al. (2017) constructed a 3D k-ω RANS-VOF model to simulate wave interaction with floating-moored OWC WECs, incorporating pre-tension mooring lines with linear springs as constrained system. In addition to NS solvers, particle-based solvers (Ferziger and PeriC, 2002; Krüger et al., 2017) have also been developed to study the OWC WECs. Zhang et al. (2025) utilized a smoothed particle hydrodynamics (SPH) model to simulate a floating OWC-breakwater system with an elastic curtain beneath it, incorporating an adaptive spacing resolution technique to reduce computational demand. Crespo et al. (2017) built up a fully 3D SPH model in DualSPHysics to predict motion responses of a real OWC prototype located at Mutriku, Spain. Their simulations were run on the GPUs (graphics processing units) to handle the complex large-scale geometries and computational domains at an affordable time cost.

Clearly, the high computational cost remains a major development bottleneck for CFD models, limiting their applicability to wave-structure interactions, particularly for a large-scale 3D case (Crespo et al., 2017). Based on IHFOAM, for example, Hu et al. (2016) performed a simulation of a floating truncated vertical cylinder under extreme waves, which required 3 days and 16 h on 32 cores for an 18 s simulation with 1.5 million cells. Wen et al. (2016) developed a 3D numerical wave basin based on a parallel-computing weakly compressible SPH model (WCSPH) to investigate wave interactions with a vertical cylinder. In their study, the wall clock time was around 5 days for a simulation of 20 s on 64 CPUs. These examples highlight that, despite adopting parallel computing frameworks, most existing wave-interaction solvers, particularly those involving FSI, still rely on relatively modest levels of parallelisation. In this regard, the Lattice Boltzmann method (LBM) demonstrates substantial potential in developing a highly scalable and computationally efficient numerical wave model. The continuous Boltzmann equation (CBE) is a simple hyperbolic equation which essentially describes the advection of the distribution function and particle velocity on a mesoscopic scale. In accordance with the recovery of macroscopic hydrodynamic behavior, Hermite series expansion (Shan et al., 2006) can be adopted to reduce continuous velocity space to a finite set of discrete velocities. It allows LBM to bypass the direct discretization of non-linear advective term, thereby simplifying the numerical implementation and enhancing computational efficiency. Furthermore, LBM inherently avoids solving the non-local pressure Poisson equation, and benefits from a highly efficient time-explicit integration scheme while it maintains second-order temporal accuracy. In the weak scaling test of Stokes wave propagation, our previous studies (Guo et al., 2025a) showed that LBM achieves near-ideal speed-up, in contrast to the linear decline in parallel efficiency observed in the SPH model by Zhu et al. (2023). Liu et al. (2021) developed a high-performance 3D LBM solver for water wave simulation, where they compared the computational efficiency and parallel scalability of their LBM solver with IHFOAM and WCSPH. Without compromising computational accuracy, the developed LBM model outperformed IHFOAM and WCSPH, achieving a speedup of 46 times that of the IHFOAM solver in the wave interaction with a land-based square cylinder. For case of wave runup on a circular island, the parallel speed-up ratio of the LBM solver can attain 80% even using 4800 CPUs, whereas the speedup ratio gradually decreased with IHFOAM when the number of CPUs exceeds 2048. Xiao et al. (2024) compared the computational efficiency between their LBM model and OpenFOAM through a dam-break flow over a small rectangular obstacle. The simulations involved 3.22 million mesh cells and 60,000 timesteps, were executed on 24 CPU cores. Results indicated that the developed LBM model achieved approximately 133 times higher computational efficiency compared to OpenFOAM, primarily due to the computationally expensive semi-implicit method for pressure-linked equations algorithm and the significant overhead from global communication in OpenFOAM.

LBM can simulate complex viscous and nonlinear effects in wave interaction with floating structures, thereby offering the potential to yield more realistic solutions with respect to an inviscid potential-flow model. However, despite its favorable computational performance, LBM remains computationally intensive, and the overall computational cost is still considerably higher than that of inviscid approaches. This limitation becomes particularly pronounced when conducting extensive parametric studies, which are essential for the optimal design, control strategy development, and performance assessment of OWC systems under varying wave conditions. Comparative studies between CFD and potential-flow solvers (Simonetti et al., 2015) have demonstrated that a potential-flow model without considering viscous effects cannot be quantitatively compared with a physical experiment. Nevertheless, their negligible computational costs make it an effective tool for rapidly identifying parameter intervals of interest through comprehensive parametric studies (Simonetti et al., 2015; Zhao and Ning, 2024). In the framework of linear potential flows, for example, Martins-rivas and Mei (2009a, 2009b) and Lovas et al. (2010) applied the matching eigenfunction expansions method (MEEM) and Galerkin approximation to study hydrodynamics of the OWCs semi-embedded in the breakwater tip, straight coast and breakwater corner, respectively. Zheng et al. (2019) derived a similar theoretical model to solve the wave interaction with the array of OWCs integrated into a straight coast. Wang et al. (2022) analytically studied a two-dimensional (2D) heaving OWC restrained by spring-damping system using the MEEM. Analytical models based on MEEM have proven to be reliable in linear wave-OWC interaction studies, offering a rapid means to uncover relationships between hydrodynamic efficiency and external conditions, such as wave frequency and turbine damping.

As highlighted in the literature review, while the LBM has demonstrated considerable potential for simulating fluid-structure interaction (FSI) in free surface flows due to its high parallel scalability and computational efficiency, its application to wave interactions with OWC WECs are scarce. Secondly, deploying OWCs in offshore regions is recognized as a promising strategy for harnessing more abundant wave energy. Nevertheless, systematic research on the floating OWCs remains relatively limited where the coupling interactions of device motion, constrained system and wave energy harvesting are not yet well-understood under the viscous flows and nonlinear wave conditions. To address these gaps, the objective of this study is to propose an efficient hierarchical modeling framework to evaluate the power extraction performance of a two-dimensional (2D) elastically constrained heave-only OWC WEC. To the best of authors' knowledge, floating OWC WECs have rarely been studied by LBM and its combination with potential-flow model, providing a novel framework for systematically and efficiently investigating wave-structure interactions in ocean renewable energy applications.

The rest of this paper is organised as follows. The LBM model and linear theoretical model are introduced in Section 2. The model validations are presented in Section 3. Then, the hydrodynamic performance of a floating OWC WEC is studied in Section 4. The paper ends with conclusions and summary in Section 5.

2. Numerical framework

2.1. Overview

The methodology begins with a linear potential-flow model, allowing for thorough and rapid parametric studies to guide computationally intensive CFD simulations. This is followed by the application of an LBM model capable of capturing real fluid effects to deliver more accurate predictions of hydrodynamic efficiency based on the optimal parameter ranges identified in the potential-flow analysis. For clarity, Fig. 1 shows a flowchart of this two-stage numerical framework.

2.2. Lattice Boltzmann model

Fig. 2 presents the 2D numerical wave tank for simulating the wave interaction with floating OWC, where C_w is the chamber width, D is the chamber draft, B is the wall thickness, C is the chamber height above still wave surface, and d is the water depth. The numerical methodology is based on our previous work (Guo et al., 2025a, 2025b) in which an interpolated bounce-back based LBM model has been successfully developed for simulating fluid-structure interaction in free surface flows.

The governing equation for fluid dynamics simulations is the multi-relaxation-time Lattice Boltzmann equation (MRT-LBE) (Guo et al., 2025b; Krüger et al., 2017), which can be expressed as follow,

$$f(\boldsymbol{x}+\boldsymbol{e}_\alpha\delta t, t+\delta t) - f(\boldsymbol{x}, t) = -\boldsymbol{M}^{-1}[\boldsymbol{S}(\boldsymbol{m}-\boldsymbol{m}^{\mathrm{eq}})] + \boldsymbol{M}^{-1}\left(\mathbf{I}-\frac{\boldsymbol{S}}{2}\right)\boldsymbol{\Phi}\delta t \tag{1}$$

where the D2Q9 velocity set illustrated in Fig. 3 is used and f_α is the discretised molecular distribution function in the α^{th} lattice direction with $\boldsymbol{e}_\alpha$ being discretised molecular velocity. δt and $\delta x = \sqrt{3}c_s\delta t$ are the time step and lattice spacing, respectively. c_s is the sound speed (Meng et al., 2013; Shan et al., 2006). $\boldsymbol{M}$ is the standard orthogonal transformation matrix mapping distributions f_α to the moment space as used (Krüger et al., 2017; Lallemand and Luo, 2000; Liu et al., 2019) and $\boldsymbol{S} = \mathrm{diag}(1,\ s_e,\ s_\epsilon, 1,\ s_q, 1,\ s_q,\ s_\nu,\ s_\nu)$ is the relaxation matrix where $s_\nu = 1/(\nu/\delta t + 0.5)$ is connected to shear viscosity and s_e, s_ϵ and s_q can be adjusted for numerical stability and accuracy. $\boldsymbol{m}^{\mathrm{eq}}$ and $\boldsymbol{\Phi}$ represent the equilibrium moment and force moment, respectively. More details regarding the orthogonalized MRT model and currently used LBM can be found in Refs. (Krüger et al., 2017; Lallemand and Luo, 2000; Liu et al., 2019) and Refs. (Guo et al., 2025b; Meng et al., 2013; Shan et al., 2006), respectively.

With regard to free surface capturing, a single-phase LBM-characterized volume-of-fluid (VOF) approach is implemented to simulate two-phase immiscible flows (Guo et al., 2025b; Korner et al., 2005). It is assumed that the lighter phase (air phase) has a negligible impact on the entire flow dynamics. Therefore, the two-phase flow is simplified to a flow with a free surface boundary. For the fluid-structure interaction, the interpolated bounce-back based approach developed in our previous studies (Guo et al., 2025b) is employed here to track floating structures in free surface flows.

Building upon the established coupling framework, to investigate the

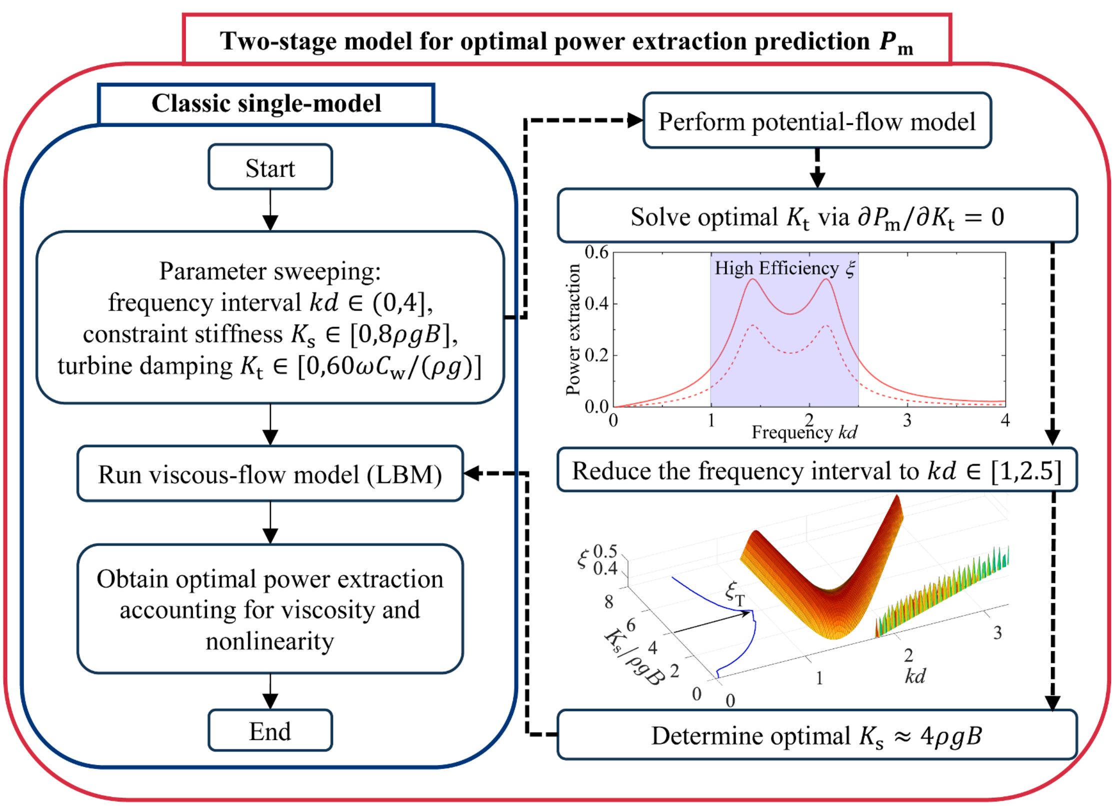

Fig. 1. Flowchart highlighting the two-stage numerical model for efficient optimization of power output.

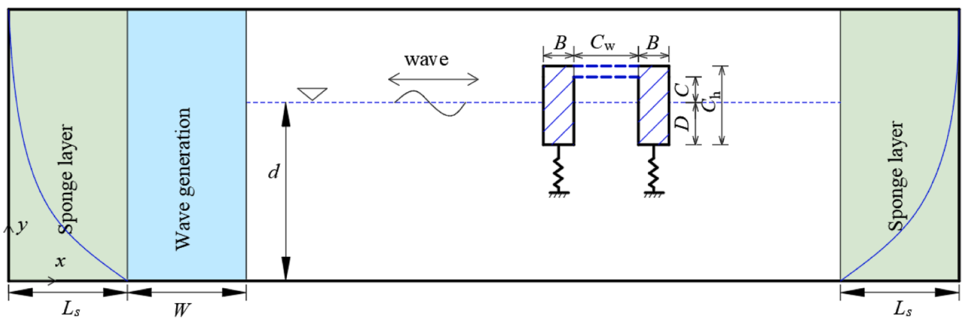

Fig. 2. Configuration of the NWT and an elastically constrained heave-only OWC WEC.

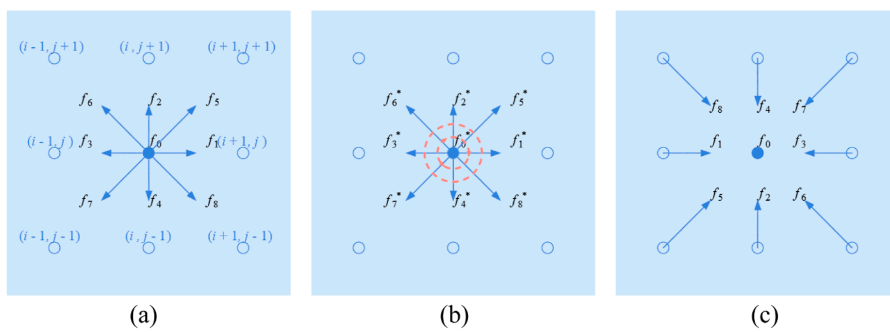

Fig. 3. Schematic diagram of the D2Q9 lattice model and LBM implementation. (a) D2Q9 lattice model, (b)collision step, and (c) streaming step, where blue circles represent eight neighboring nodes and blue arrows are the eight discrete velocities e_α; f_α^* is the post-collision DF.

wave dynamics, the more specific add-on modules including the momentum source method and perfectly matched layer (PML) technique, are incorporated to generate and absorb the waves, respectively. The second order Stokes waves are generated by introducing the following source term (Choi and Yoon, 2009; Liu et al., 2019) into governing equation,

$$\begin{cases} S_{g,x} = g(2\beta(x - x_s))e^{-\beta(x-x_s)^2}\dfrac{\delta}{A\omega}(A_1\cos\theta + A_2\cos 2\theta) \\ S_{g,y} = 0 \end{cases} \tag{2}$$

where $\beta = 20/W^2$ is related to source width W; $\theta = \frac{\pi}{2} - \omega t - \arcsin\left(\left(-A_1 + \sqrt{A_1^2 + 8A_2^2}\right)/(4A_2)\right)$; x_s is the centre of wave generation area and δ is distribution source density,

$$\delta = \frac{2A(\omega^2 - \alpha_1 g k^4 d^3)}{\omega I k(1 - \alpha(kd)^2)} \tag{3}$$

where A is the first order wave amplitude; $A_1 = A$ and $A_2 = \frac{A^2 k \cosh kd}{4\sinh^3 kd}\left(1 + 2\cosh^2 kd\right)$; $\alpha = -0.38{,}955$ and $\alpha_1 = \alpha + 1/3$ is a coefficient of the basic Boussinesq equation; k and ω are the wavenumber and angular frequency, respectively; $I = \sqrt{\pi/\beta}e^{-k^2/4\beta}$.

In NWT works, a numerical damping layer is a reliable technique to absorb those outgoing waves. Classically, an equivalent damping force related to the local fluid velocity as formulated by Darcy' law can be implemented to attenuate waves (Choi and Yoon, 2009; Liu et al., 2019; Liu et al., 2015). However, waves may be reflected by the damping layer itself as they propagate through the layer (Higuera et al., 2013). In this study, a Perfectly Matched Layer (PML) (Najafi-Yazdi and Mongeau, 2012), which is more effective in absorbing waves, is applied for non-reflection at the interface between the absorbing layer domain and the interior domain. Based on the derivation of PML for a linear hyperbolic PDE, PML as an additional collision term can be incorporated into LBE directly (Stoll, 2014),

$$f(\boldsymbol{x} + \boldsymbol{e}_\alpha \delta t, t + \delta t) - f(\boldsymbol{x}, t) = \Omega_{\mathrm{PML}}\delta t - \boldsymbol{M}^{-1}[\boldsymbol{S}(\boldsymbol{m} - \boldsymbol{m}^{\mathrm{eq}})] + \boldsymbol{M}^{-1}\left(\mathbf{I} - \frac{\boldsymbol{S}}{2}\right)\boldsymbol{\Phi}\delta t \tag{4}$$

$$\Omega_{\mathrm{PML}}(x, t) = -\sigma\left(2f_{\mathrm{P}}^{\mathrm{eq}} + \sigma Q + \boldsymbol{e}\cdot\nabla\mathscr{S}\right) \tag{5}$$

where σ is the damping coefficient, $\frac{\partial\mathscr{S}}{\partial t} = f_{\mathrm{P}}^{\mathrm{eq}}$ and $f_{\mathrm{P}}^{\mathrm{eq}}$ is the perturbation component of equilibrium distribution function, that is,

$$f^{\mathrm{eq}} = f_{\mathrm{P}}^{\mathrm{eq}} + f_{\mathrm{s}}^{\mathrm{eq}} \tag{6}$$

where $f_{\mathrm{s}}^{\mathrm{eq}}$ can be computed from the hydrostatic water condition and then $f_{\mathrm{P}}^{\mathrm{eq}}$ can be known.

The damping coefficient can be expressed as,

$$\sigma = \sigma_{\max}\frac{e^{\left|\frac{x - x_0}{L_s}\right|^{n_s}} - 1}{e - 1} \tag{7}$$

where $\sigma_{\max}$ and n_s are empirical coefficients, and x_0 is the starting location of the PML. L_s is the length of the PML. One-step trapezoid time integration is implemented to calculate $\mathscr{S}$ from $f_{\mathrm{P}}^{\mathrm{eq}}$ and the second order central difference scheme is applied to the linear advection term $\boldsymbol{e}\cdot\nabla\mathscr{S}$ in the PML interior domain. More implementation details can be found in Ref. (Najafi-Yazdi and Mongeau, 2012; Stoll, 2014).

2.3. Potential-flow model

In this section, we briefly summarize the classical potential-flow formulation. This is included for completeness and clarity, so that the paper is self-contained and the assumptions, notation, and baseline model used in the subsequent analysis are clearly defined. Fig. 4 shows a schematic of the floating 2D OWC WEC. In the framework of linear potential flow theory, the governing equation and boundary conditions

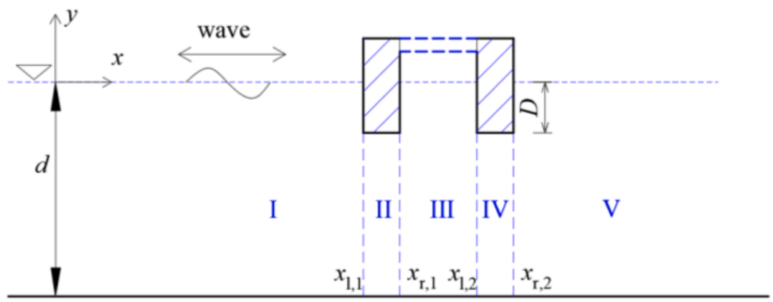

Fig. 4. Schematic of a heave-only floating OWC device in which the five subdomains and geometrical parameters used in the theoretical model are presented.

of this boundary value problem can be expressed as (Guo et al., 2025b; Wang et al., 2022),

$$\nabla^2\phi_n = \frac{\partial^2\phi_n}{\partial x^2} + \frac{\partial^2\phi_n}{\partial y^2} = 0 \tag{8}$$

$$\begin{cases} \dfrac{\partial\phi_n}{\partial y} = \dfrac{\omega^2}{g}\phi_n + \begin{cases} \dfrac{\mathrm{i}\omega}{\rho g}\delta_{n,4}, & x_{\mathrm{r},i} \le x \le x_{\mathrm{l},i+1},\ y = 0 \\ 0, & x \le x_{\mathrm{l},1},\ \ x \ge x_{\mathrm{r},2},\ y = 0 \end{cases} \\ \dfrac{\partial\phi_n}{\partial x} = -\mathrm{i}\omega\left(\delta_{n,1} + (y - y_0)\delta_{n,3}\right) \quad x = x_{\mathrm{l},i}, x = x_{\mathrm{r},i},\ -D \le y \le 0 \\ \dfrac{\partial\phi_n}{\partial y} = 0, \quad y = -d \\ \dfrac{\partial\phi_n}{\partial y} = -\mathrm{i}\omega\left(\delta_{n,2} - (y - y_0)\delta_{n,3}\right) \ x_{\mathrm{l},i} \le x \le x_{\mathrm{r},i},\ y = -D \\ \lim\limits_{x\to\pm\infty}\left\{\dfrac{\partial}{\partial x} \mp \mathrm{i}k\right\}(\phi_0 - \phi_{\mathrm{inc}}, \phi_1 \sim \phi_4) = 0 \end{cases} \tag{9}$$

where, $x_{\mathrm{r},i}$ and $x_{\mathrm{l},i}$ are the x coordinates of right and left surface for the i^{th} wall; The total velocity potential is expressed as $\phi = \sum_{n=0}^{4}\zeta_n\phi_n$ in which $\phi_0 = \phi_D$ and ϕ_n $(n = 1 \sim 4)$ are the diffraction and radiation potentials; $\phi_1 \sim \phi_3$ and ϕ_4 are the radiation potentials induced by the body motions of OWC (i.e., surge (x-translation), heave (y-translation), and pitch (z-rotation) motions), and inner pressure drop inside the OWC chamber, respectively; ρ and g are the water density and gravity acceleration, respectively.

Satisfying the continuous pressure and velocity between the adjacent subdomains, and applying the orthogonality of vertical eigenfunctions, a set of linear algebraic equations can be derived to determine those unknown coefficients by substituting Eqs. (A.1) - (A.5) into continuity conditions. More details can be found in Appendix and Refs. (Guo et al., 2020; Guo et al., 2021; Zheng et al., 2020).

2.4. Power take-off model

The hydrodynamic model based on LBM has been established and thoroughly validated in our previous study, and it is capable of tracking the body motion of a floating OWC without a PTO system. A PTO system, such as a Wells turbine, generates a reacting air pressure inside the OWC chamber above the free surface. To simulate the PTO effect, following Josset and Clément (2007), the air pressure can be estimated by a pneumatic model. It is assumed that the air inside the chamber is an ideal gas and follows the isentropic compression process. Also, a Wells turbine characterized by linear relation between air flow rate and pressure drop across the turbine is applied in this power-take-off model. Following the derivation (Josset and Clément, 2007), the air pressure inside the chamber is evaluated by the following equation,

$$\frac{\dot{p}_{\mathrm{a}}(t)}{p_{\mathrm{a}}(t)} = \gamma\left[-\frac{K_{\mathrm{t}}(p_{\mathrm{a}}(t) - p_{\mathrm{a}0})}{V_a(t)}\left(1 - \varsigma\frac{\rho_{\mathrm{a}}(t) - \rho_{\mathrm{a}0}}{\rho_{\mathrm{a}}(t)}\right) - \frac{\dot{V}_a(t)}{V_a(t)}\right] \tag{10}$$

where p_{a} is the air pressure inside the chamber, $\dot{p}_{\mathrm{a}}$ is the time derivation of p_{a}. γ is the heat capacity ratio of air and $p_{\mathrm{a}0}$ is the atmospheric pressure outside the chamber. $\rho_{\mathrm{a}}(t)$ and $\rho_{\mathrm{a}0}$ are the air density and reference air density, respectively. V_a and $\dot{V}_a$ denote the chamber volume and its change rate, respectively. It can be observed that the present pneumatic model takes the air compressibility into consideration, which turns out to significantly affect the energy harvesting for large-scale OWCs (Mia et al., 2023). Revising surrounding atmospheric pressure of free surface boundary condition, the air pressure inside the chamber is reacted to the hydrodynamic model, the hydrodynamics and aerodynamics are then two-way coupled.

The turbine damping K_{t} quantifies the linear relation between volume flow rate and pressure drop $\Delta p = p_{\mathrm{a}} - p_{\mathrm{a}0}$ in the Wells turbine, that is to say,

$$Q(t) = -K_{\mathrm{t}}\Delta p \tag{11}$$

where Q is the air volume flow rate through the turbine. Since the air in or out the chamber involves different air density, ς is an indicator generalizing the two processes (air in and air out),

$$\begin{cases} \varsigma = 0, & Q \le 0 \\ \varsigma = 1, & Q > 0 \end{cases} \tag{12}$$

An implicit backward Euler scheme is applied to discretize Eq. (10) for numerical stability. For a uniform time step δt and discrete indices $n \to n+1$, $\dot{p}_{\mathrm{a}}$ is evaluated at the new time moment and the geometrical quantities and air density at t^n are used, it obtains,

$$p_{\mathrm{a}}^{n+1} = p_{\mathrm{a}}^n - \delta t\gamma p_{\mathrm{a}}^{n+1}\left[\frac{K_{\mathrm{t}}(p_{\mathrm{a}}^{n+1} - p_{\mathrm{a}0})}{V_a^n}\left(1 - \varsigma\frac{\rho_{\mathrm{a}}^n - \rho_{\mathrm{a}0}}{\rho_{\mathrm{a}}^n}\right) + \frac{\Delta V_a}{\delta t V_a^n}\right] \tag{13}$$

where $\Delta V_a = V_a^{n+1} - V_a^n$. With the definitions of coefficients A and B, a quadratic equation is obtained,

$$A = \frac{\gamma\delta t K_{\mathrm{t}}}{V_a^n}\left(1 - \varsigma\frac{\rho_{\mathrm{a}}^n - \rho_{\mathrm{a}0}}{\rho_{\mathrm{a}}^n}\right),\ B = \frac{\gamma\Delta V_a}{V_a^n} \tag{14}$$

$$A\left(p_{\mathrm{a}}^{n+1}\right)^2 + (B - Ap_{\mathrm{a}0} + 1)p_{\mathrm{a}}^{n+1} - p_{\mathrm{a}}^n = 0 \tag{15}$$

In contrast to the fully nonlinear air-compressibility formulation used in the LBM model, the linear isentropic relationship $c_{\mathrm{a}}^2\dot{\rho}_{\mathrm{a}} = \dot{p}_{\mathrm{a}}$ ($\gamma = 1$) is adopted in the potential-flow model (Martins-rivas and Mei, 2009), and the nonlinear terms in Eq. (10) are linearized accordingly,

$$\frac{\dot{p}_{\mathrm{a}}}{\rho_{\mathrm{a}0}c_{\mathrm{a}}^2} = \frac{-K_t(p_{\mathrm{a}} - p_{\mathrm{a}0}) - \dot{V}_a}{V_{\mathrm{a}0}} \tag{16}$$

Once $\Delta p^{n+1} = p_{\mathrm{a}}^{n+1} - p_{\mathrm{a}0}$ is determined, one can estimate the instantaneous and averaged pneumatic power extracted by the OWC WEC,

$$P_{\text{cap}}(t) = Q(t)|\Delta p| = K_{\text{t}}(\Delta p)^2 \tag{17}$$

$$P_{\text{m}} = \frac{1}{N}\sum_{n=1}^{N} P_{\text{cap}}(t) \tag{18}$$

where N is the number of discrete time steps within a single wave period T.

Moreover, to quantify how effectively the wave energy converter captures the incoming wave energy, a dimensionless parameter, the hydrodynamic efficiency, is defined as,

$$\xi = \frac{P_{\text{m}}}{P_{\text{inc}}} \tag{19}$$

where P_{inc} represents the averaged energy flux per unit width.

2.5. Coupled heave motion and pressure response

For a 2D symmetric OWC, similar to the symmetric flow pattern induced by the internal pressure oscillation, the heave motion generates symmetric fluid flows, whereas the other degrees of freedom, i.e., surge and pitch motions produce antisymmetric flows. Such antisymmetric flows do not effectively contribute to constructive or destructive changes in the air chamber volume and therefore have no significant influence on power absorption. In view of this, the present work focuses exclusively on heave-only floating OWCs.

The heave motion of OWC induced by waves is solved by,

$$m_{\text{s}}\ddot{\boldsymbol{Y}} = \boldsymbol{F}_y + m_{\text{s}}\boldsymbol{g} + K_{\text{s}}\boldsymbol{Y} \tag{20}$$

where m_{s} and $\boldsymbol{Y}$ are the mass and motion response of the rigid body, respectively; $\ddot{\boldsymbol{Y}} = \boldsymbol{a}_{\text{s}}$ and $\dot{\boldsymbol{Y}} = \boldsymbol{u}_{\text{s}}$ are the acceleration and velocity of OWC with heave motion. $\boldsymbol{F}_y$ is the vertical wave force including two components: the wave loads acted on the wet surface of OWC and the air pressure force above water surface inside the chamber. The external forces also include the gravity $m_s\boldsymbol{g}$ and spring forces $K_s\boldsymbol{Y}$, where K_s is the spring stiffness.

When the heave motion of OWC is involved, the volume change rate should also take the contribution of the heave velocity into account. In turn, the oscillating air pressure also induces an additional force on the OWC structure. The solving procedure for the coupled heave motion and pressure response during the simulation of floating OWC-wave interaction within each computational time step as follows: After the MRT-LBE is solved, the free surface model is implemented to update the air-water interface. Then GIMEM is applied to calculate $\boldsymbol{F}_y$ required in Eq. (20) and the solid position and velocity based on the equation of motion are updated. Finally, the air pressure inside the chamber is computed and updated based on the pneumatic model (Eq. (10)) once the volume change rate of the OWC chamber $\dot{V}_a$ is evaluated.

In the potential-flow model, under the linearized assumption and following our previous studies (Guo et al., 2021), the simultaneous coupled equation for heave motion Eq. (20) and inner pressure drop Eq. (16) can be expressed as,

$$\boldsymbol{F}_{\text{e}} = \left[-\omega^2(\boldsymbol{M}_{\text{s}} + \boldsymbol{\mu}) - \text{i}\omega(\boldsymbol{\lambda} + \boldsymbol{\lambda}_{\text{PTO}}) + (\boldsymbol{K} + \widetilde{\boldsymbol{K}})\right]\boldsymbol{\zeta} = (\boldsymbol{\Lambda} - \text{i}\omega\boldsymbol{\lambda}_{\text{PTO}})\boldsymbol{\zeta} \tag{21}$$

i.e.,

$$\begin{bmatrix} F_{\text{e}} \\ \dfrac{q_{\text{e}}}{\text{i}\omega} \end{bmatrix} = \left[-\omega^2\left(\begin{bmatrix} M & 0 \\ 0 & \dfrac{a_{\text{PTO}}}{\omega^3} \end{bmatrix} + \begin{bmatrix} \mu_{2,2} & \mu_{2,4} \\ \mu_{4,2} & \mu_{4,4} \end{bmatrix}\right) + \begin{bmatrix} K_{2,2} & K_{2,4} \\ K_{4,2} & K_{4,4} \end{bmatrix} + \begin{bmatrix} K_s & 0 \\ 0 & 0 \end{bmatrix} - \text{i}\omega\left(\begin{bmatrix} \lambda_{2,2} & \lambda_{2,4} \\ \lambda_{4,2} & \lambda_{4,4} \end{bmatrix} + \begin{bmatrix} 0 & 0 \\ 0 & \dfrac{K_{\text{t}}}{\omega^2} \end{bmatrix}\right)\right]\begin{bmatrix} \zeta_2 \\ \zeta_4 \end{bmatrix}$$

where $a_{\text{PTO}} = \frac{\omega V_{\text{a0}}}{\rho_{\text{a0}} c_{\text{a}}^2}$, and $\zeta_4 = \Delta p$, $\boldsymbol{M}_{\text{s}}$, $\boldsymbol{\mu}$, $\boldsymbol{\lambda}$, $\boldsymbol{K}$, and $\widetilde{\boldsymbol{K}}$ are the mass, added mass, radiation damping, hydrostatic restoring, and spring stiffness matrices, respectively. The optimal turbine damping $K_{\text{t}} = c_{\text{opt}}$ is theoretically expressed as,

$$\frac{\partial P_{\text{m}}}{\partial K_{\text{t}}} = 0 \rightarrow c_{\text{opt}} = \omega\left|\det\left(\frac{\boldsymbol{\Lambda}}{\Lambda_{1,1}}\right)\right| \tag{22}$$

where $\Lambda_{i,j}$ represents the element of matrix $\boldsymbol{\Lambda}$ located in the i^{th} row and the j^{th} column.

3. Model validation

Due to the limited availability of experimental studies on 2D (or equivalent 2D) floating OWCs, two experimental cases, where the structure span is equal to the width of wave flume, are combined to validate the reliability of the proposed numerical model on predicting wave-structure interaction. These experiments include an offshore stationary OWC device (Iturrioz et al., 2015) and pile-restrained floating box (Ning et al., 2016) subjected to waves, corresponding to the hydrodynamic model and pneumatic model in Section 2.2 and 2.4. For the potential-flow model, the theoretical energy conservation relation is adopted for validation as shown in Appendix.

3.1. Wave generation and absorption

Numerical tests of monochromatic waves in a two-dimensional flume with a constant water depth of 0.2 m are first carried out to validate the wave-generation and absorption functions. The length and height of this numerical wave tank are 18 m and 0.24 m, respectively. The uniform grid size is set to 0.004 m. The computational results using momentum source method from the present LBM model and NS-based model (Choi and Yoon, 2009) are compared with each other. As conducted in Ref. (Choi and Yoon, 2009), the wave generation source region is positioned at the center of the NWT, while sponge layer source regions are placed at both ends for wave absorption. The wave parameters used in Eq. (2) are set to a period of 1 s and amplitudes of $A = 0.005$, 0.01, 0.015, and 0.03 m to generate the respective target waves. Fig. 5 presents the water surface displacement for different wave amplitudes at time instant $t = 23$ s. In comparison with second-order analytical solutions, the Stokes waves generated by both the present LBM model and the NS-based model agree well outside the source region, with negligible dissipation observed along the propagation direction. As the wave nonlinearity increases from $A/d = 0.025$ to 0.15, the wave shape becomes asymmetric with a sharper crest and a flatter trough, similar to Cnoidal waves.

Fig. 6 shows the vertical distribution of horizontal (x-) u and vertical (y-) v velocities of Stokes waves with a wave amplitude of 0.005 m at the time instant $t = 23$ s, in which $x = 0$ corresponds to a wave crest in the propagating region. It can be observed that the predicted results have good agreement with the second-order analytical solutions below the still water level. The slight discrepancy in vertical component arises from the fact that the vertical velocity is sensitive to phase error when its magnitude is small.

Fig. 7 displays the free surface elevation predicted by the present model compared with the analytical solution. In this case, the PML is applied at the left end of the domain, while the right end is a solid wall boundary. The wave generation region is located adjacent to the PML. A train of monochromatic waves of amplitude $A = 0.01$ m and period $T = 1$ s is generated, and the superposition of incident and reflected waves from right wall results in the formation of standing waves. The numerical results present that the wave absorption works well in which the outgoing waves are gradually absorbed when they propagate through the PML, and the resulting standing waves agree well with analytical solutions.

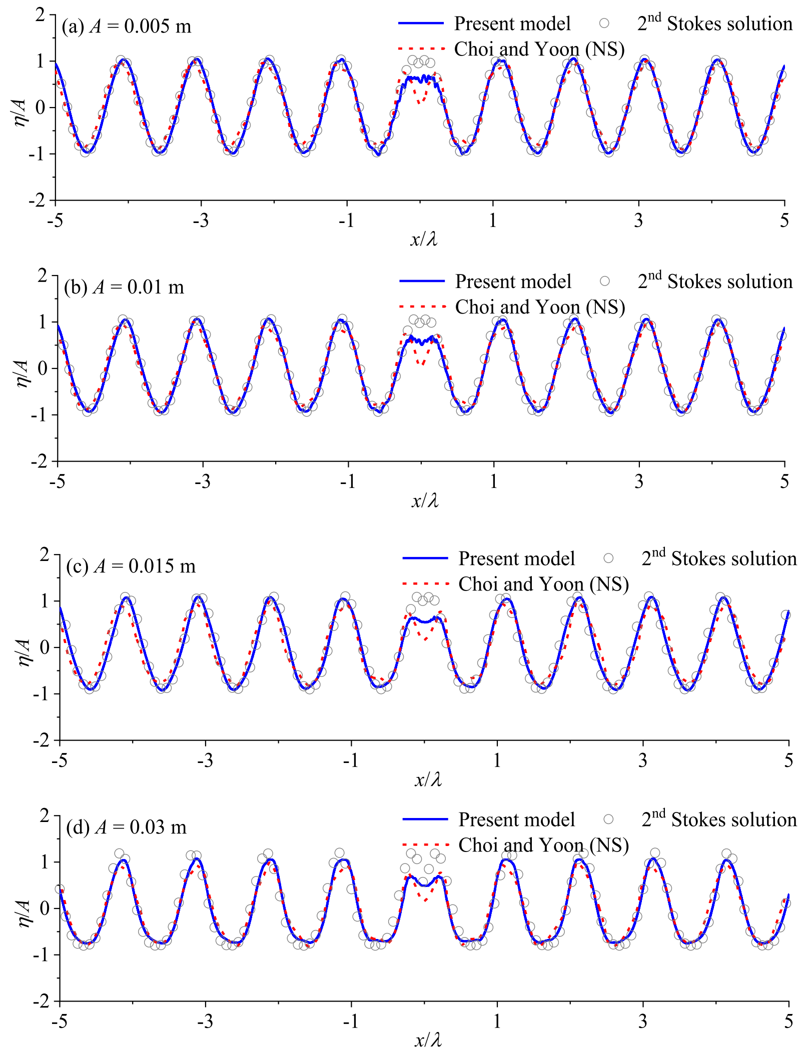

Fig. 5. Water surface displacement using the present LBM model, NS-based model (Choi and Yoon, 2009), and second-order analytical solution (A = 0.005, 0.01, 0.015, and 0.03 m, T = 1 s), with a constant water depth of 0.2 m (PML at the both ends).

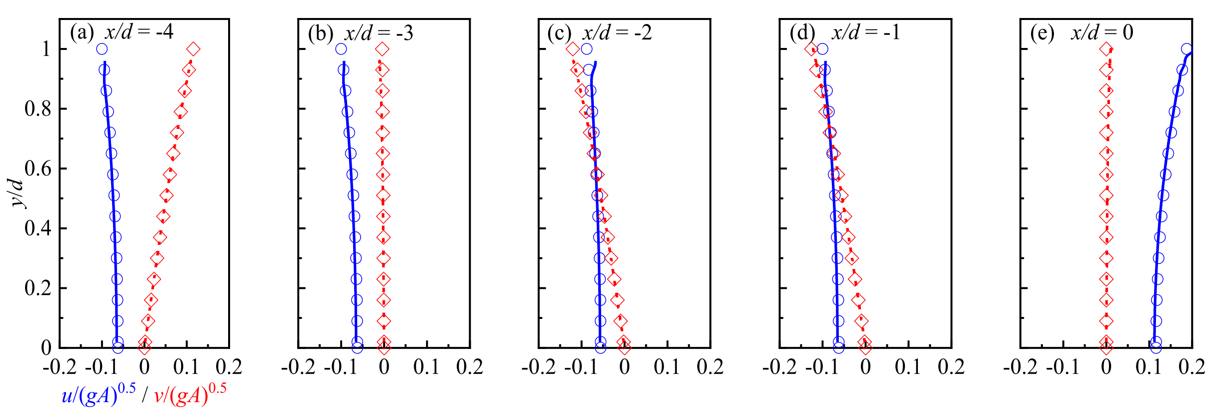

Fig. 6. Vertical distribution of horizontal velocity u and vertical velocity v using the present LBM model and second-order analytical solutions (A = 0.005 m, T = 1 s), where line and symbol representations denote the velocities from present the LBM model and analytical solution, respectively, with $x = 0$ specified as the position of the wave crest.

3.2. A stationary OWC under waves: pneumatic model validation

To replicate the experimental case conducted by Iturrioz et al. (2015), an offshore stationary OWC device is placed in the NWT as sketched in Fig. 8 and the geometrical parameters of the device are listed in Table 1. The simulation involves regular waves with a period of T = 1.3 s and 1.7 s and wave height H = 0.08 m. The uniform mesh size is $H/27$. In the following numerical simulations, for better numerical

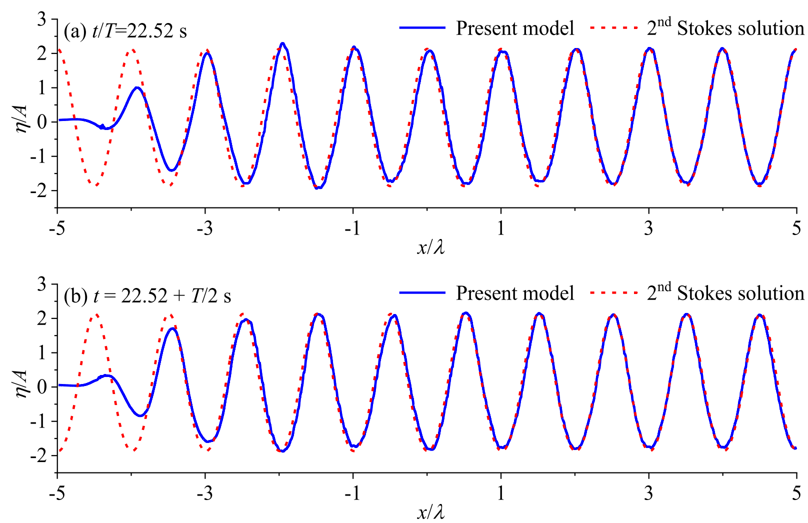

Fig. 7. Water surface displacement using the present LBM model and linear analytical solution (A = 0.01 m, T = 1 s), with a constant water depth of 0.2 m (PML at the left end and wall boundary at the right end).

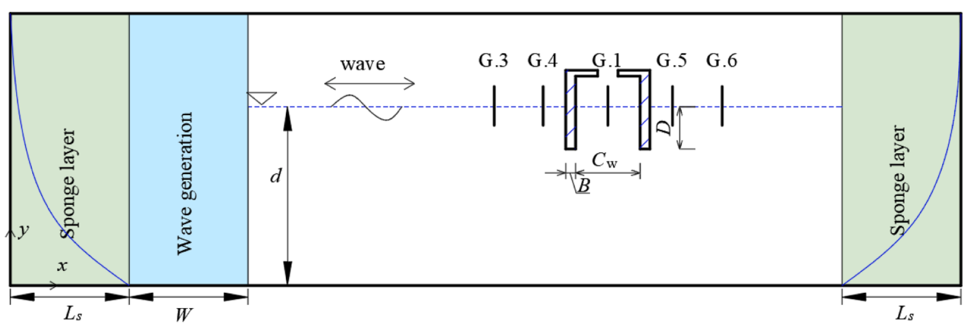

Fig. 8. Sketch of the NWT and an offshore stationary OWC placed inside.

Table 1
The Geometrical parameters of NWT and the OWC device.

Waves	T (s)	H (m)	d (m)	NWT	Length (m)	Height (m)
	1.3, 1.7	0.08	0.6		10L	1.5d
Wave Absorption	$\sigma_{\max}$ (s^{-1})	n_s	L_s (m)	Wave Generation	W (m)	
	6.67	2	2L		L	
OWC	D (m)	B (m)	C_w (m)	Sub-grid model	C_s	
	0.2	0.02	0.3		0.1	

where C_s denotes the Smagorinsky coefficient in the sub-grid turbulent model (Guo et al., 2025a) and wave absorption parameters are heuristically chosen according to pure-wave tests to minimize reflected waves.

stability, the recommended relaxation rates are used (Guo et al., 2025b; Liu et al., 2021), i.e., $\boldsymbol{S} = \mathrm{diag}(1,\ 0.3,\ 1, 1, 1, 1, 1,\ s_\nu,\ s_\nu)$. Unlike a pneumatic model to simulate the air dynamics, the experiment (Iturrioz et al., 2015) employed a top orifice to represent the air turbine. To ensure comparability with the experimental data, the turbine damping K_t in the present numerical model is calibrated based on achieving an identical pressure drop between the numerical and experimental results. After this calibration, wave elevations inside the OWC chamber obtained from the numerical model are compared with the experimental data to validate the accuracy of the LBM model.

Following the observation from Iturrioz et al. (2015), the pressure drop in the chamber is negligible if the top orifice is set as 0.05 m. This case allows the present single-phase LBM model without an air turbine to be compared with experimental results. Fig. 9 shows the time histories of free surface elevation recorded by a series of wave gauges at the same locations as in the experiment. It can be observed that a partially standing wave mode is caused by the wave reflection at the seaside of OWC and transmitted wave is smaller than the incident wave. The nonlinear wave deformation, peaks and troughs at different measurement locations follow similar characteristics to the experimental results (Iturrioz et al., 2015), validating the capability of present numerical model on predicting the wave motion. Furthermore, Fig. 10 illustrates the free surface elevation at the chamber center for different pressure drops, equivalent to a top orifice of 0.009 m and 0.05 m, respectively. The good agreement between numerical and experimental results confirms the reliability of the pneumatic model implemented in this study.

3.3. A heave-free box under waves: LBM validation

In comparison with the published results (Isaacson et al., 1998; Mia et al., 2023; Ning et al., 2016), the heave motion response of a rectangular box under regular waves is numerically investigated to validate the developed NWT based on LBM. The box-shaped floating body has a height H_b of 0.6 m and breadth B of 0.8 m. Its draft D is 0.2 m. Table 2

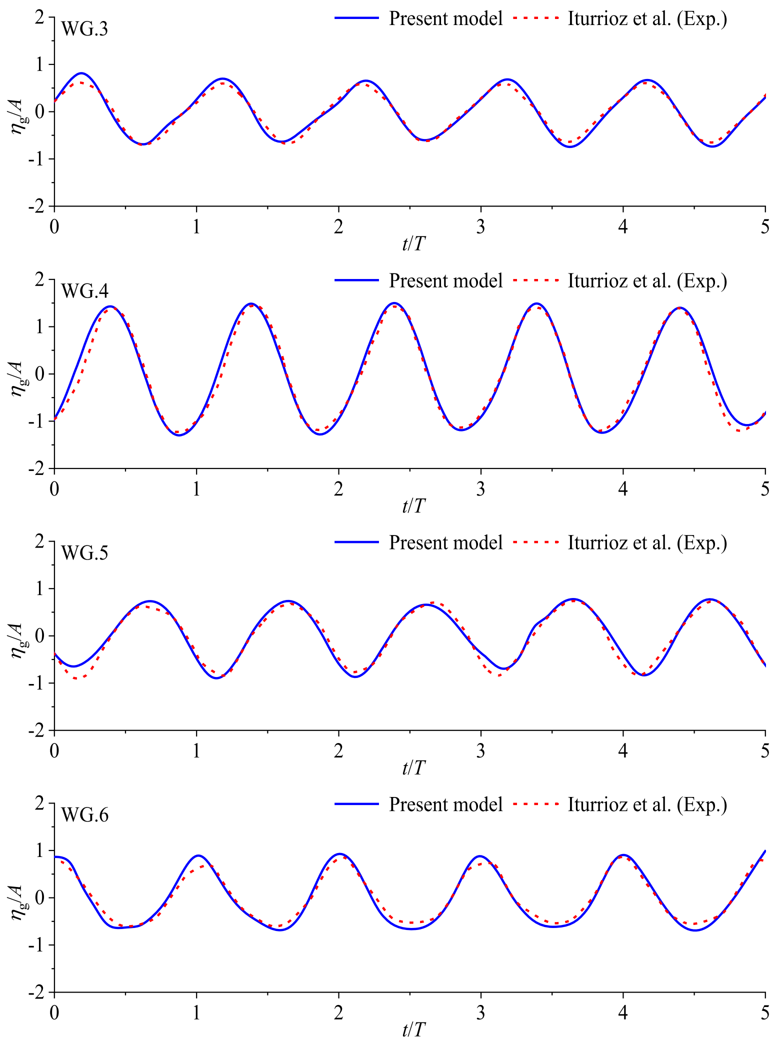

Fig. 9. Comparisons of free surface elevation outside the chamber between experiments (Iturrioz et al., 2015) and the present numerical model, subject to incident waves $T = 1.7$ s and $H = 0.08$ m.

lists all parameters of box and wave conditions, keeping the same NWT as used in Section 3.1. The present uniform mesh size is $H/40$. Fig. 11 shows the sketch of NWT and the box which is allowed to float in heave mode only. The heave motion of the box under waves with different wave frequencies and constant wave amplitude is depicted in Fig. 12. The present numerical results show a good agreement with other numerical and experimental results, demonstrating the capability of the developed model on predicting the wave-induced motion.

4. Hydrodynamic efficiency of a heave-only OWC WEC

Combined with linear potential-flow solutions, the developed LBM model is implemented to study the power extraction of an elastically constrained heave-only OWC. As sketched in Fig. 2, the OWC chamber height above the mean water surface C is 0.1 m and the chamber height C_h is 0.378 m. Wave conditions and geometry sizes of the OWC are listed in Tables 3 and 4, respectively. The relevant parameters of the simulation domain and wave generation & absorption are the same as those listed in Table 1.

Although the present study focuses on regular waves, the proposed framework is not fundamentally restricted to regular-wave conditions. It consists of two complementary components, namely a theoretical potential-flow model for rapid parametric screening and an LBM-based numerical model for more physically detailed simulations. In the theoretical component, irregular waves can be incorporated through the linear superposition of multiple regular wave components with random phases, an approach that has already been successfully applied in our previous semi-analytical studies of OWC systems under irregular waves in Refs. (Gang et al., 2022; Guo et al., 2025c). In the numerical LBM component, following Ref. (Choi and Yoon, 2009) the extension is also straightforward: the regular-wave input can be replaced by irregular wave trains constructed from the same superposition, and the corresponding momentum source term can be reformulated accordingly. Therefore, the present two-part framework is readily extensible to irregular-wave simulations.

4.1. Spatial and temporal convergence study

A mesh dependency study is conducted to demonstrate that the selected mesh is fine enough to obtain converged numerical results for wave interaction with the floating OWC. In this study, the spring stiffness and turbine damping are set to $K_s/(\rho g B) = 4$ and $\rho g K_t/(\omega C_w) = 0.285$, respectively. According to the linear potential flow model established, the resonant frequency of OWC on the heave motion is around $kd = 2.1$ for the specific geometry and dynamic setup. Therefore, the mesh dependency study is carried out under the regular wave with $kd = 2.1$ and $H = 0.024$ m. Fig. 13 presents the velocity fields and the free surface elevation around the heaving OWC at different time

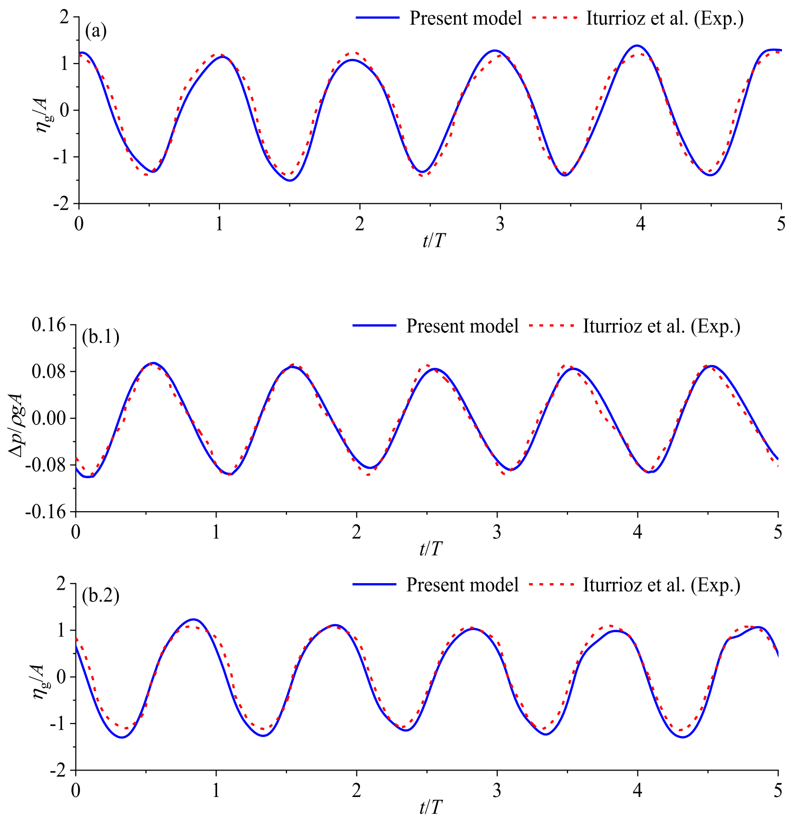

Fig. 10. Comparisons of free surface elevation inside the chamber between experiments (Iturrioz et al., 2015) and the present numerical model, subjected to incident waves $T = 1.3$ s and $H = 0.08$ m. (a) Equivalent case to a top orifice of 0.05 m and (b) Equivalent case to a top orifice of 0.009 m.

Table 2
The parameters for freely-heaving box interacting with waves.

Waves	B/L (m)	T (s)	H (m)	d (m)	Boxes	D (m)	B (m)	H_b (m)
	0.1~0.37	1.18~2.75	0.2	1		0.2	0.8	0.6

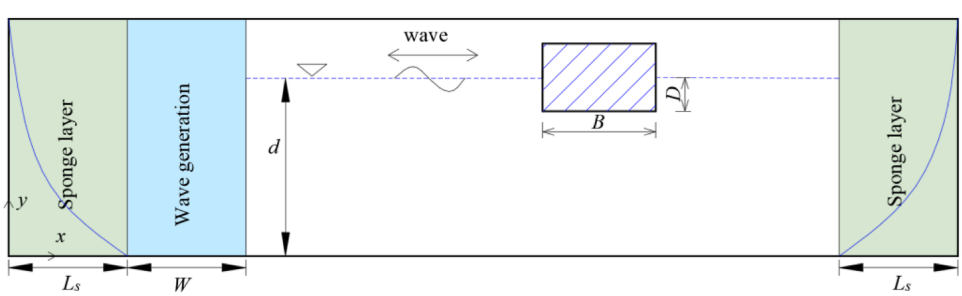

Fig. 11. Sketch of the NWT and a rectangular floater placed inside.

instants, clearly capturing the dynamic oscillation of the internal water column in response to the passing wave troughs and crests. Setting three spatial and temporal resolutions, the time histories of pressure drop inside the chamber and heave motion over five wave periods are compared with each other, shown in Fig. 14 and Fig. 15, respectively. Little discrepancy is observed between coarse and fine results, indicating that the converged numerical solutions are obtained with $\delta x = C_w/80$ and $\delta t = T/34000$.

Following the model validation and mesh dependency study, the effects of spring stiffness, turbine damping, and wave height on the hydrodynamic performance of heave-only OWC WEC are then investigated by the developed hybrid models combining LBM and MEEM.

In the present study, c_{opt} denotes the theoretically derived optimal turbine damping obtained from Eq. (22), whereas K_t denotes the turbine damping coefficient implemented in the pneumatic model of the LBM solver, as described in Section 2.4. In other words, c_{opt} is first evaluated from the theoretical model and then used to define the practical turbine damping input K_t. Since the implemented damping is subject to an upper limit for practical considerations, K_t is taken as the bounded form of c_{opt}, namely

$$\rho g K_t/(\omega C_w) = \min(60, \rho g c_{opt}/(\omega C_w)) \tag{23}$$

Therefore, when the theoretical optimum satisfies the practical limit, $K_t = c_{opt}$; otherwise, K_t is capped at the corresponding upper-bound

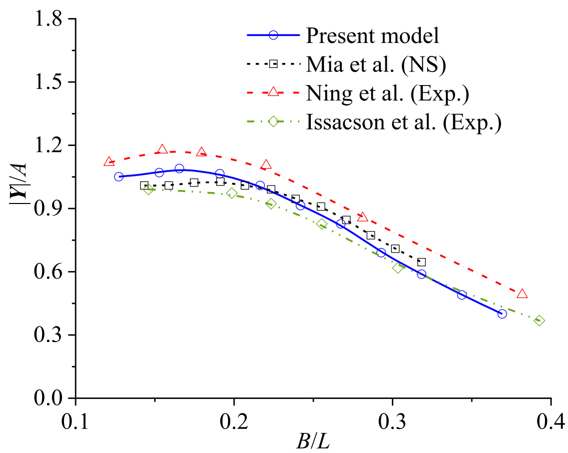

Fig. 12. Comparison of heave amplitude between LBM and published numerical and experimental results (Isaacson et al., 1998; Mia et al., 2023; Ning et al., 2016).

Table 3
Wave conditions for the study of heave-only OWC in Fig. 2, with a wave height of $H = 0.024$ m.

kd	0.8	1.0	1.2	1.3	1.4	1.5	1.6	1.7
T (s)	1.95	1.63	1.42	1.34	1.27	1.22	1.17	1.12
kd	1.8	1.9	2.0	2.1	2.2	2.3	2.4	2.5
T (s)	1.087	1.05	1.02	0.99	0.97	0.94	0.92	0.90

Table 4
Geometrical parameters of OWC device in Fig. 2.

d (m)	C_w (m)	C_h (m)	B (m)	C (m)	D (m)
0.5	0.2	0.378	0.1	0.1	0.252

value.

4.2. Effect of spring stiffness

The effect of spring stiffness on power extraction is systematically studied through the theoretical potential-flow model at first. Fig. 16 displays the optimal hydrodynamic efficiency ξ and optimal turbine damping c_{opt} as functions of wave frequency kd and spring stiffness K_s. In Fig. 16(a), the highlighted region ($\xi \geq 0.35$) is identified as the valuable power extraction region, and the solid blue line represents the total hydrodynamic efficiency $\xi_T = \int \xi d(kd)$ within the valuable frequency interval, as a function of K_s. It can be observed that the free-floating OWC, i.e., K_s =0, cannot effectively harness wave energy. As the spring stiffness increases, the valuable frequency interval broadens and then splits into two distinct regiones. The systematic parameter analysis reveals that the peak frequency region of ξ lies within $1 \leq kd \leq 2.5$ and the optimal spring stiffness is around $K_s/(\rho g B) = 4$ where ξ_T reaches its peak. Guided by these theoretical findings, wave conditions within the valuable frequency region are selected for further investigations using the LBM model, as listed in Table 3, with a focus on the heaving OWC at $K_s/(\rho g B) = 4$. Moreover, Fig. 16(b) shows that c_{opt} near first peak frequency of ξ increases with increasing K_s. This highlights the necessity of dynamically adjusting turbine damping for floating OWCs with varying spring stiffness to achieve optimal power extraction, rather than relying on constant damping values derived from stationary OWC configurations.

In LBM model, Fig. 17 compares the turbine damping K_t and hydrodynamic efficiency ξ of three types of constrained OWCs, i.e., fixed ($K_s = \infty$), heave-free floating ($K_s = 0$), and elastically constrained ($K_s = 4\rho g B$) cases. For the fixed case, both K_t and ξ show a local peak around kd =1.4, corresponding to the fluid motion resonance inside the chamber. This fluid resonance also induces peaks for the heave-free floating and elastically constrained OWCs near kd =1.4. However, the elastically constrained ($K_s = 4\rho g B$) case stands out by exhibiting an additional local peak at kd =2.1, attributed to the heave resonance of OWC structure. As described in Eq. (21), the coupled heave motion and inner fluid motion are considered as an oscillating system with two degrees of freedom under the excitation of incident waves. This oscillating mass-damping-stiffness system thus presents two natural frequencies: one corresponding to inner fluid motion resonance and the other to the heave motion resonance of OWC. The natural frequencies explain the double-peak behavior observed in Fig. 16(a) and Fig. 17(b) for $K_s = 4\rho g B$. Consistent with the conclusions of the theoretical model, the heave-free floating ($K_s = 0$) case is not a feasible option for power extraction and the elastically constrained ($K_s = 4\rho g B$) case offers a broader valuable frequency region than the fixed case, which is particularly advantageous for power extraction in real sea conditions characterized by waves of varying frequencies.

At kd =1.4, Fig. 18 further illustrates the effects of K_s on volume flow rate through PTO system, with the contributions from heave motion and interior fluid motion defined as Q_1 and Q_2, respectively. As spring stiffness K_s increases, the heave motion of OWC naturally decreases, leading to a reduction in Q_1 as shown in Fig. 18(a). Conversely, the volume flow rate Q_2, contributed by interior fluid motion, increases with increasing K_s in Fig. 18(b). One notable phenomenon is that the coupled interaction between the heave motion and interior fluid motion introduces a phase difference in both Q_1 and Q_2 across the three constraint cases. For instance, the phase difference in Q_2 between heave-free floating ($K_s = 0$) and fixed ($K_s = \infty$) OWCs approaches π as illustrated in Fig. 18. In addition, for $K_s = 0$, there is a significant phase difference between Q_1 and Q_2, which leads to a reduced total net volume flow rate Q, as depicted in Fig. 18(c). This in fact indicates that, for $K_s = 0$, the heave motion of OWC and interior fluid motion are approximately in-phase, which cannot effectively compress the volume of air chamber and is hence not favorable for power extraction.

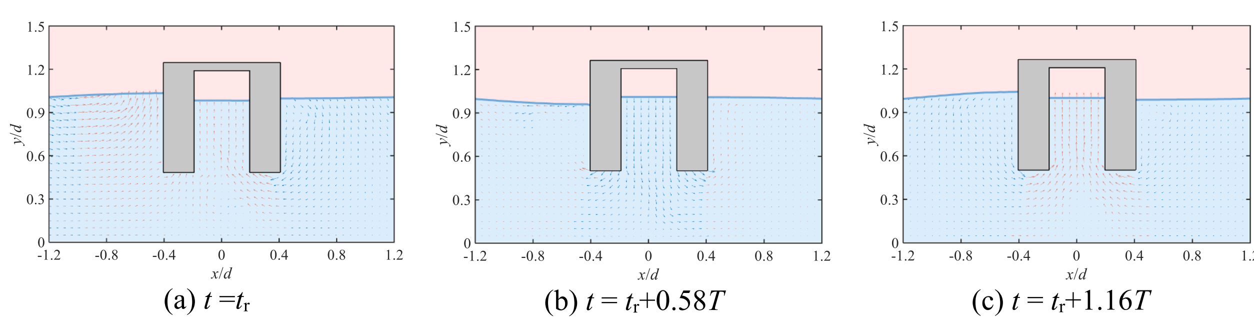

Fig. 13. Velocity field and free surface profile around the OWC at three instants with spatial and temporal resolutions of $\delta x = C_w/80$ and $\delta t = T/34000$ (The red and blue arrows indicate vertical fluid velocities above and below zero, respectively).

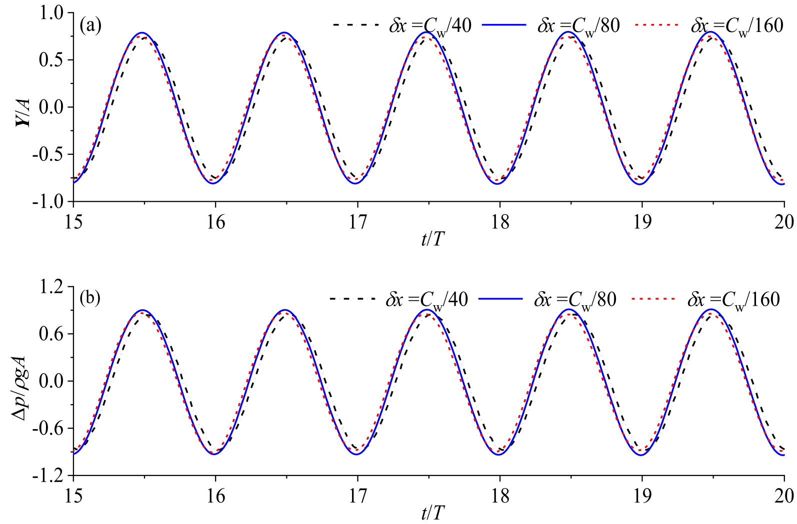

Fig. 14. Time histories of the dimensionless pressure drop and heave motion for different spatial resolutions at kd =2.1. (a) heave motion $\boldsymbol{Y}$ and (b) pressure drop Δp.

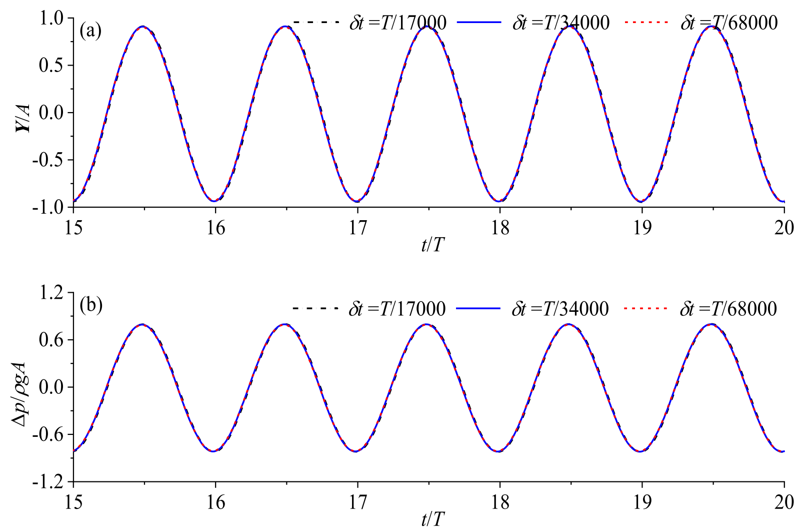

Fig. 15. Time histories of the dimensionless pressure drop and heave motion for different temporal resolutions at kd =2.1. (a) heave motion $\boldsymbol{Y}$ and (b) pressure drop Δp.

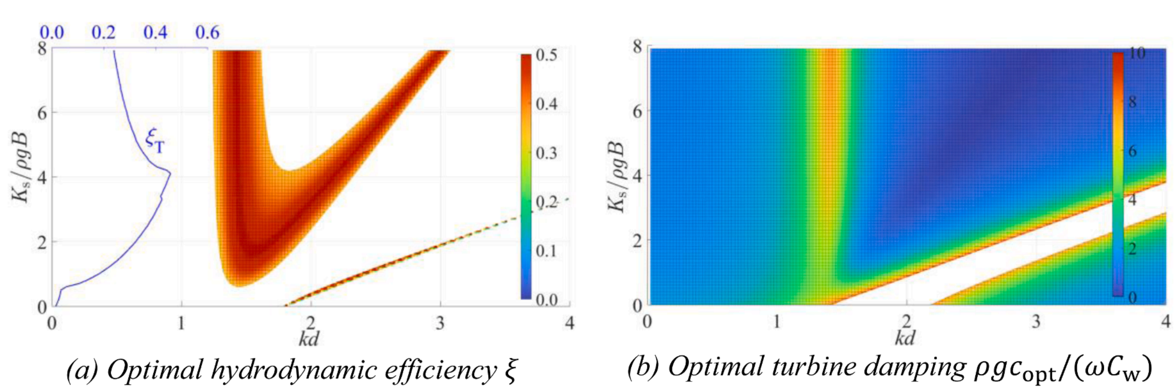

Fig. 16. Frequency response of optimal hydrodynamic efficiency and optimal turbine damping versus the spring stiffness for the heave-only OWC, based on potential-flow model.

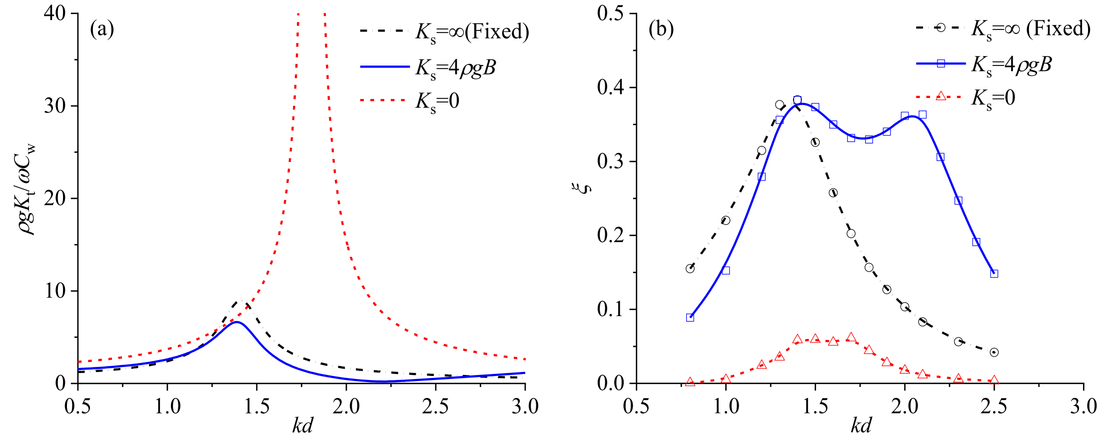

Fig. 17. Frequency responses of the turbine damping and hydrodynamic efficiency of the heave-only OWC in LBM model. (a) Turbine damping K_t that is determined as c_{opt} derived from the potential-flow model, and (b) hydrodynamic efficiency ξ.

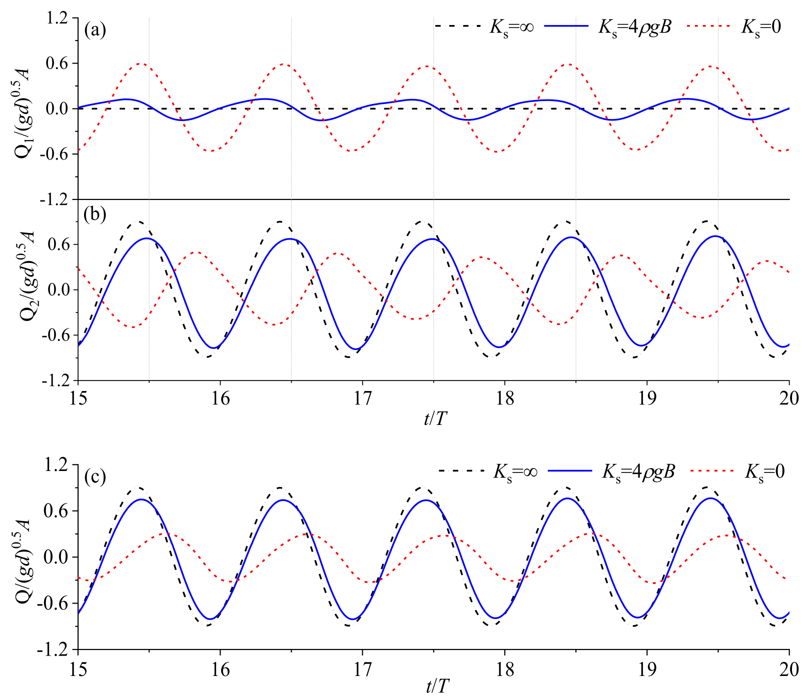

Fig. 18. Time history of volume flow rate under different constraints at kd=1.4. (a) Q_1 attributed to the OWC motion, (b) Q_2 attributed to fluid motion inside the OWC chamber, and (c) total volume flow rate Q.

4.3. Effect of turbine damping

In this section, we investigate the effect of turbine damping K_t on hydrodynamic performance of the elastically constrained OWC with $K_s = 4\rho gB$, and evaluate the feasibility of theoretical prediction for the optimal turbine damping in the developed LBM solver. Fig. 19 illustrates the time histories of pressure drop Δp, volume flow rate Q, and power output P_{cap} for three values of K_t at the fluid resonance frequency kd =1.4. Δp shows an opposite trend to Q, against K_t. Compared with the cases of $K_t = 4c_{opt}$ and $K_t = 0.25c_{opt}$, the OWC with $K_t = c_{opt}$ obviously captures more wave energy. It can also be observed from Fig. 19(c) that the peaks marked by rectangular symbols are higher than those marked by circle symbols, indicating an asymmetry between air inhalation and exhalation. Similar results can also be found in Ref. (Luo et al., 2014; Simonetti et al., 2018). This characteristic may be attributed to the nonlinear deformation of waves and the different air density involved between inhalation and exhalation as expressed by Eq. (12).

Fig. 20 presents the time histories of volume flow rate Q_1 and Q_2 at kd =1.4 and 2.1. In terms of the magnitude, Q_2 which is contributed by water surface motion, dominates over, Q_1 which is induced by the OWC motion, at the interior fluid resonance frequency kd =1.4 in Fig. 20(a). Conversely, at the heave resonance frequency kd =2.1, the amplitude of Q_2 and Q_1 are approximately comparable in Fig. 20(b). For both frequencies kd =1.4 and 2.1, Q_1 increases with the decrease of K_t, due to the increase of pressure $|\Delta p|$ as shown in Fig. 19(a). The variation in Q_2, however, depends on the dominant excitation. To be specific, at kd =1.4, the dominant excitation is the fluid motion inside the chamber due to the interior fluid resonance. As $|\Delta p|$ increases with the decrease of K_t (see Fig. 19(a)), the intensified pressure restricts the up-and-down water surface inside the chamber, leading to a decrease of Q_2 in Fig. 20 (a.2). In contrast, the amplitude of Q_2 at kd =2.1 increases with the decrease of K_t in Fig. 20 (b.2), which is due to that the dominant excitation of volume flow rate is the heave motion of OWC due to its heave resonance.

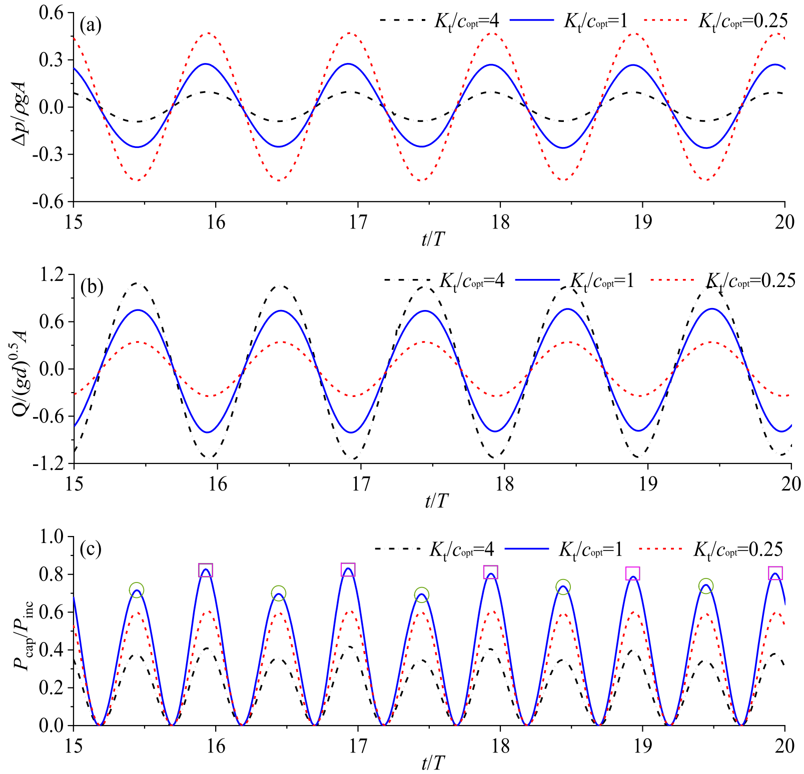

Fig. 19. Time histories of pressure drop, volume flow rate and power output for different turbine damping at kd=1.4. (a) Pressure drop Δp, (b) volume flow rate Q, and (c) power output P_{cap}.

In addition, Fig. 20(c) illustrates the phase difference $\Delta\theta$ between Q_1 and Q_2 as a function of K_t at kd =1.4 and 2.1. For both frequencies, $\Delta\theta$ increases with the decrease of K_t. This phenomenon indicates that the wave motion generally tends to be in-phase with the heave motion of OWC as K_t decreases, which contributes to a reduction in the total net volume flow rate Q.

Fig. 21 further illustrates the frequency response of heave amplitude $|\boldsymbol{Y}|$ and hydrodynamic efficiency ξ of the present LBM and potential-flow models. In both potential-flow and LBM models, $|\boldsymbol{Y}|$ follows the same trends versus kd for each K_t, and it increases with the decrease of K_t at each frequency. ξ of the floating OWC with $K_t = c_{opt}$ is the highest compared with the OWC using $K_t = 4c_{opt}$ and $K_t = 0.25c_{opt}$. Due to the absence of viscosity and nonlinearity, the potential-flow model tends to overestimate the heave motion response around kd =2.1, and this overestimation becomes more pronounced with the decrease of K_t in Fig. 21(a). Similar situations also occur in the hydrodynamic efficiency illustrated in Fig. 21(b).

In addition, ξ of OWC with $K_t = 4c_{opt}$ and $K_t = 0.25c_{opt}$ are identical to each other in the established theoretical model, which results from the linearized hydrodynamic and pneumatic models. To be specific, Substituting the pressure drop, $\Delta p = q'/\left[a + \mathrm{i}\left(b - kc_{opt}/\omega\right)\right]$ derived from the linearized coupling Eq. (21), into the theoretical time-averaged power P_m, P_m can be expressed as:

$$P_m = \frac{1}{2}\left(kc_{opt}\right)|\Delta p|^2 = \frac{1}{2}\frac{|q'|^2}{\left(k + \frac{1}{k}\right)\frac{c_{opt}}{\omega^2} - 2b\frac{1}{\omega}} \tag{24}$$

where $k = K_t/c_{opt}$, $q' = \frac{q_e}{\mathrm{i}\omega} - F_e\frac{S_{21}}{S_{11}}$, $a = \mathrm{Re}\left\{S_{22} - \frac{S_{21}S_{12}}{S_{11}}\right\}$, and $b = \mathrm{Im}\left\{S_{22} - \frac{S_{21}S_{12}}{S_{11}}\right\}$. It is noted that $c_{opt}^2 = \omega^2\left(a^2 + b^2\right)$ from Eq. (22). Therefore, the hydrodynamic efficiency for $K_t = k_1c_{opt}$ and $K_t = k_2c_{opt}$ are the same if k_1 is the reciprocal of k_2.

As a result of nonlinear and viscous effects, the present LBM model does not follow this equivalence relation, especially near the resonance frequencies kd =1.4 and 2.1 as shown in Fig. 21(b). Reducing the nonlinearity and turbulence allows numerical solutions from LBM to approach potential-flow solutions: Increasing the inner pressure amplitude $|\Delta p|$ suppresses the dominant fluid motion inside the chamber at kd =1.4 (inner fluid resonance frequency), while decreasing $|\Delta p|$ restrains the dominant heave motion of OWC at kd =2.1 (heave motion resonance frequency). This explains why ξ for $K_t = 0.25c_{opt}$ (i.e., with higher $|\Delta p|$) is closer to the corresponding potential-flow solutions at kd =1.4, while ξ for $K_t = 4c_{opt}$ (i.e., with lower $|\Delta p|$) approaches the theoretical solutions at kd =2.1 in Fig. 21(b).

Based on the discussions above, the linear potential-flow model can identify the characteristic frequency regions where ξ reach the local peaks (i.e., at around kd =1.4 and 2.1). However, it overestimates hydrodynamic efficiency. The LBM model with the capability of simulating nonlinear and viscous effects provides more reliable results.

In Section 4.2, c_{opt} from the theoretical model is used as the baseline and applied to the LBM model. To evaluate whether c_{opt} is the optimal turbine damping for the LBM model, Fig. 22 illustrates the heave motion response $|\boldsymbol{Y}|$ and absolute deviation $\left(\xi - \xi_{c_{opt}}\right)/\xi_{c_{opt}}$ versus K_t/c_{opt} under three wave frequencies, kd =1.4, 1.8, and 2.1, where $\xi_{c_{opt}}$ represents the hydrodynamic efficiency under the condition of $K_t = c_{opt}$. Following previous observations, increasing $|\Delta p|$ at kd =1.4 by using a slightly smaller K_t reduces the nonlinear and viscous effects, resulting in the highest ξ (5.2% greater than $\xi_{c_{opt}}$). Conversely, decreasing $|\Delta p|$ at kd =2.1 by using a slightly larger K_t mitigates these effects, leading to the highest ξ (0.9% greater than $\xi_{c_{opt}}$). Although the maximum hydrodynamic efficiency does not occur at $\xi_{c_{opt}}$ using $K_t = c_{opt}$ due to viscosity and nonlinearity, the deviation is relatively small for the tested wave conditions, as shown in Fig. 22(b), where the largest deviation is 5.2%.

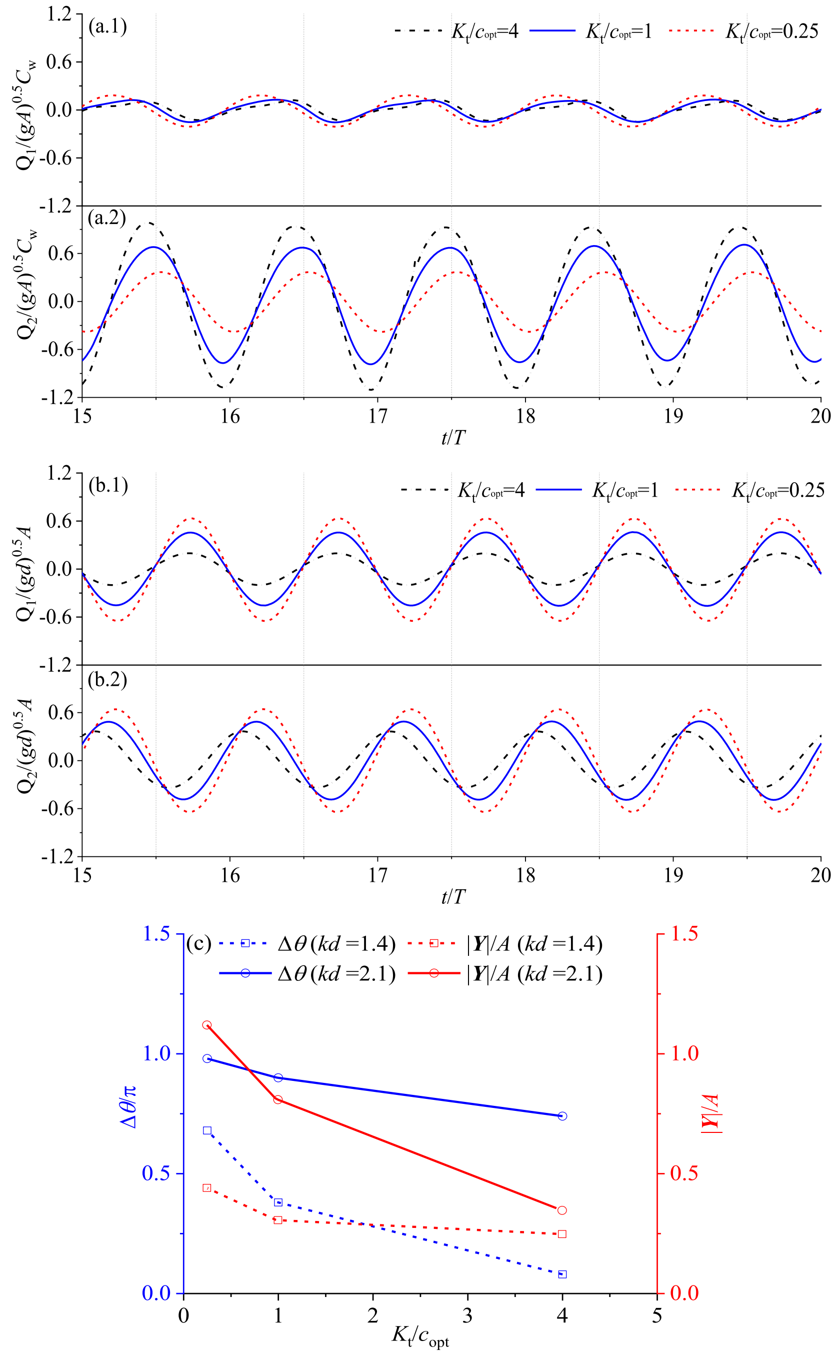

Fig. 20. (a) Time histories of Q_1 and Q_2 at wave frequencies kd =1.4, (b) time histories of Q_1 and Q_2 at wave frequencies kd =2.1, and (c) the phase difference between Q_1 and Q_2 for different turbine damping.

This suggests that c_{opt} from theoretical model is a feasible prediction for the optimal turbine damping in a viscous flow model.

4.4. Effect of incident wave height

The nonlinear and viscous impacts are further studied, comparing the simulation results of three incident wave heights $H/d = 0.048$, 0.096, and 0.144. Setting as $K_s/(\rho gB) = 4$ and $K_t = c_{opt}$, Fig. 23 shows the frequency response of dimensionless quantities, i.e., pressure amplitude $|\Delta p|/(\rho gA)$, volume flow rate $|Q|/\left(\sqrt{gd}A\right)$, heave amplitude $|\boldsymbol{Y}|/A$, and hydrodynamic efficiency ξ, in the present LBM and potential-flow models for different H. As H/d increases, these dimensionless quantities decrease, where the peaks of ξ are 0.38, 0.32, and 0.27 for $H/d = 0.048$, 0.096, and 0.144, respectively. They are obviously smaller than ξ predicted by the potential-flow model. This discrepancy can be attributed to the fact that increasing H amplifies the nonlinear and viscous effects.

For clarity, the vorticity fields near the floating OWC interacted with waves at different wave heights are depicted in Fig. 24 to discuss the viscous effects, where the vorticity is defined as $\boldsymbol{\omega}_z = \nabla \times \boldsymbol{u}$. Each row of figures represents the vortex evolution over one period of OWC motion. During a heave motion period, four pairs of vortices with opposite directions are generated at the sharp corners when waves propagate through the bottom edge of the OWC walls, with the upstream vorticity intensity naturally larger than the downstream. They then separate from

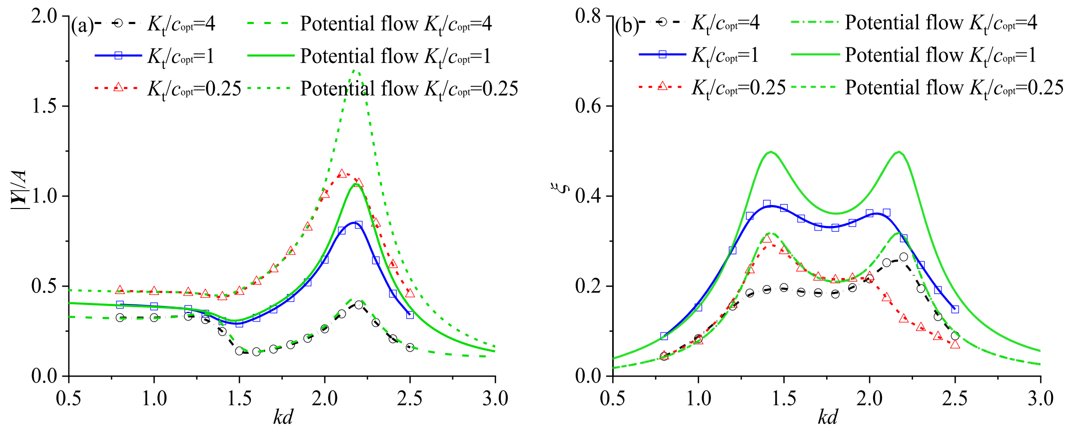

Fig. 21. Frequency response of heave motion and hydrodynamic efficiency of OWC using different turbine damping (a) Heave amplitude $|\boldsymbol{Y}|$ and (b)hydrodynamic efficiency ξ.

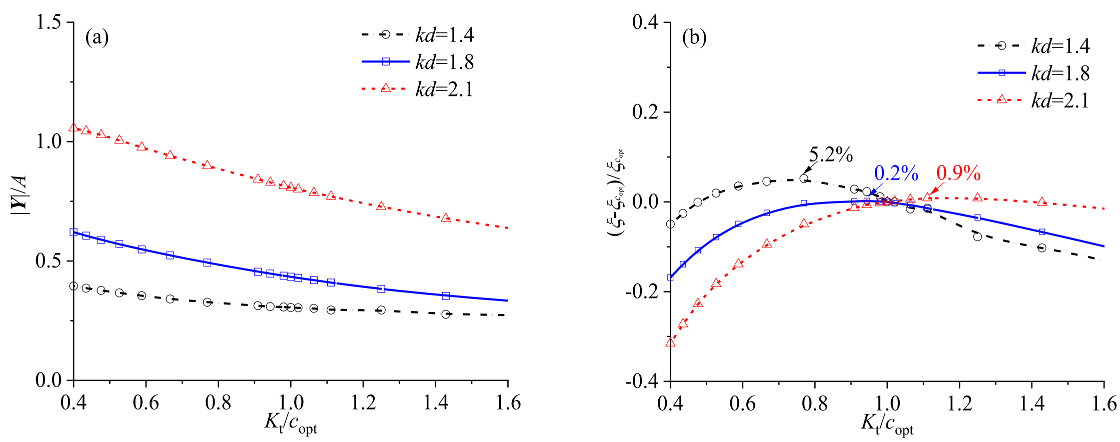

Fig. 22. Variations of heave response, and absolute deviation of ξ against $\xi_{c_{opt}}$ $(K_t = c_{opt})$ versus turbine damping at kd=1.4, 1.8 and 2.1. (a) Heave amplitude $|\boldsymbol{Y}|$, and (b) absolute deviation $\left(\xi - \xi_{c_{opt}}\right)/\xi_{c_{opt}}$.

the bottom end of OWC and gradually dissipate.

To quantify this viscous effect, two indicators are evaluated at kd=1.4. An instantaneous vorticity-based indicator is introduced to measure the local vortical activity near the OWC opening,

$$I_\omega = \frac{1}{A_v}\int_{A_v} \omega_z^2 dA \tag{25}$$

where A_v denotes the selected region around the lower opening, defined as $-0.6 \le x/d \le 0.6$, $-0.2 \le y/d \le 0.8$. Although this instantaneous quantity does not represent the total viscous dissipation over one wave period, it provides a useful measure of the relative intensity of local vortical motion near the opening. the section-averaged horizontal velocity is used to evaluate the effective exchange flow beneath the OWC opening,

$$\overline{u}_{\rm sec} = \frac{1}{L_{\rm sec}}\int_{L_{\rm sec}} u dy \tag{26}$$

where $L_{\rm sec}$ denotes the selected vertical section beneath the OWC opening.

The calculated values are summarized in Table 5. As H/d increases from 0.048 to 0.144, I_ω increases from 6.37 to 71.03, confirming that the vortical activity and local shear near the OWC opening are greatly intensified under larger waves. In contrast, $\overline{u}_{\rm sec}/A$ decreases from 13.37 to 11.13, indicating that the effective volume flux per unit incident wave amplitude becomes weaker. Therefore, although larger waves provide stronger excitation, a larger portion of the flow energy is associated with local vortical motion and separated flow near the opening, rather than being effectively converted into coherent chamber-scale oscillation. This reduces the effective internal water-column motion and the associated pneumatic response, which is consistent with the decrease in those quantities shown in Fig. 23.

The regularity of the pneumatic response is further examined using the peak and trough envelopes of the chamber pressure, as shown in Fig. 25. For $H/d = 0.048$, the pressure peaks and troughs remain nearly constant over measured periods, indicating a regular pressure response. As H/d increases, more evident cycle-to-cycle fluctuations appear, especially for $H/d = 0.144$. This behavior is considered to be associated with the unsteady nature of vortex shedding.

Overall, intensified and unsteady vortex shedding at larger wave heights affects the OWC performance by enhancing local viscous losses near the openings, weakening the effective inflow, and introducing stronger cycle-to-cycle fluctuation of the chamber pressure response. These combined effects reduce the portion of incident wave energy converted into useful pneumatic power, thereby contributing to the lower hydrodynamic efficiency.

In addition to the viscous effect, the nonlinear effect on ξ is also analyzed by the Fast Fourier Transform (FFT) with Hanning window applied to the time series of surface elevations near the OWC. Fig. 26 illustrates the amplitude spectrum of surface elevation in- and out-side the OWC chamber for different H at kd =1.4, 1.8 and 2.1, where wave

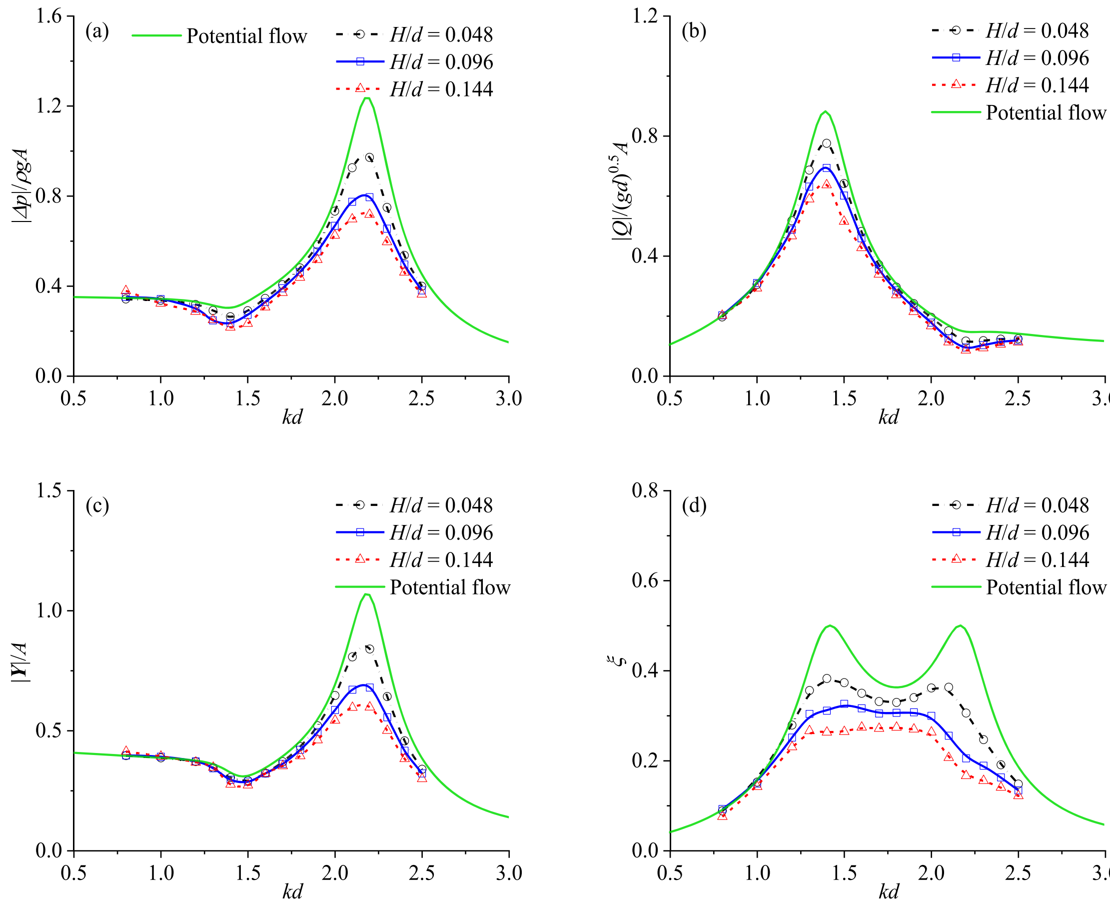

Fig. 23. Frequency response of pressure drop, volume flow rate, heave motion, and hydrodynamic efficiency of OWC for different wave heights H. (a) Pressure amplitude inside the chamber $|\Delta p|$, (b) volume flow rate $|Q|$, (c) heave amplitude $|\boldsymbol{Y}|$, and (d) hydrodynamic efficiency ξ.

gauges G_o and G_i are located at 0.05 m upstream of the chamber and at the chamber center, respectively. At each wave frequency, the second-order harmonic wave component increases with incident wave heights H both inside and outside the chamber, and the second-order harmonic wave component outside the chamber is larger than those inside the chamber. It can be concluded that the wave energy in the first-order primary waves is transferred to the second-order waves when waves interact with the OWC. Due to the weak transmission ability of short waves, most second-order waves outside the chamber are reflected from the OWC wall. Also, the weak energy conversion ability inherent to the short waves means the second-order waves inside the chamber cannot be effectively absorbed by this WEC. Therefore, the increase in wave nonlinearity with incident wave heights leads to an increase in the second-order harmonic component, which also contributes to a reduction in hydrodynamic efficiency.

At this stage, the present analysis provides an overall assessment of the second-order harmonic components, while a quantitative separation of the bound and free second-order harmonics remains limited. Such an analysis would be critical for more targeted optimization of OWC performance. As the present study focuses primarily on methodological development, a detailed wave-decomposition analysis is beyond its current scope. In future work, a wave decomposition method will be applied for refined hydrodynamic analysis.

4.5. Computational efficiency

To assess the computational efficiency of the present LBM model, two representative problems are selected to compare with OpenFOAM model established by Zhuang et al. (2024): the wave propagation case in Section 3.1 and the wave-OWC interaction case in Section 4, including both stationary and floating OWC configurations. The same computational domain, spatial resolution, temporal step, and physical parameters are adopted in both the LBM and OpenFOAM simulations to ensure a consistent comparison. Table 6 summarizes the wall-clock time of OpenFOAM and the present LBM model using different numbers of CPU cores. AMD EPYC™ 7002 series processors are used in both simulations, specifically the EPYC 7742 for the LBM and the EPYC 7532 for the OpenFOAM.

For the wave propagation case, the OpenFOAM simulation requires around 3 days using 128 CPU cores, whereas the LBM spent 17 h under the same core number, corresponding to a speed-up of approximately 4.2 times. This improvement is mainly attributed to the explicit time-marching procedure and the local collision-streaming operations in the LBM, which avoid the solution of a global pressure Poisson equation. In terms of parallel scalability, the LBM model achieves speed-ups of 3.86 and 7.25 when the number of CPU cores is increased by factors of 4 and 8, corresponding to parallel efficiencies of 96% and 90%, respectively.

For the wave-OWC interaction cases, the present LBM model also demonstrates good computational efficiency and parallel scalability. Under the same 128-core configuration, the LBM simulation is approximately 4.6 times faster than OpenFOAM for the stationary OWC case. As the number of CPU cores increases, the wall-clock time of both stationary and floating OWC simulations decreases consistently, with parallel efficiencies remaining above 86% at the highest tested core counts. The floating OWC case is more expensive than the stationary case due to the additional fluid-structure interaction treatment and moving-boundary update. Overall, these results show that the present LBM

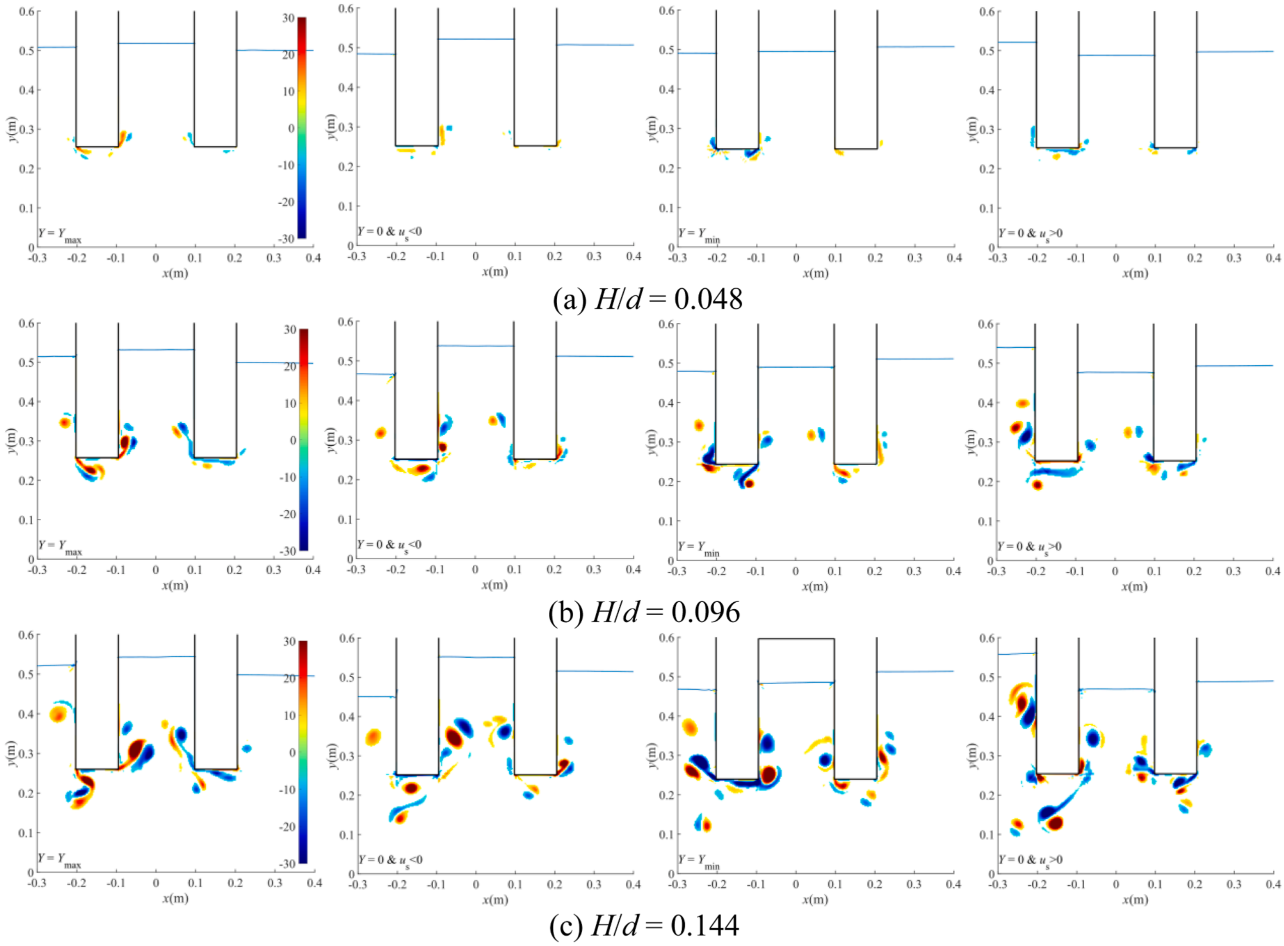

Fig. 24. Vorticity fields near the floating OWC for different wave heights H for kd =1.4 at four instants: $Y = Y_{max}$, $Y = 0$ & $u_s > 0$, $Y = Y_{min}$, and $Y = 0$ & $u_s < 0$, where $\boldsymbol{Y} = Y\boldsymbol{j}, \boldsymbol{u}_s = u_s\boldsymbol{j}$.

Table 5
I_ω and $\bar{u}_{sec}$ for different incident wave heights at kd =1.4 and $Y = Y_{max}$.

	$H/d = 0.048$	$H/d = 0.096$	$H/d = 0.144$
I_ω	6.37	30.09	71.03
$\bar{u}_{sec}$ /A	13.37	12.29	11.13

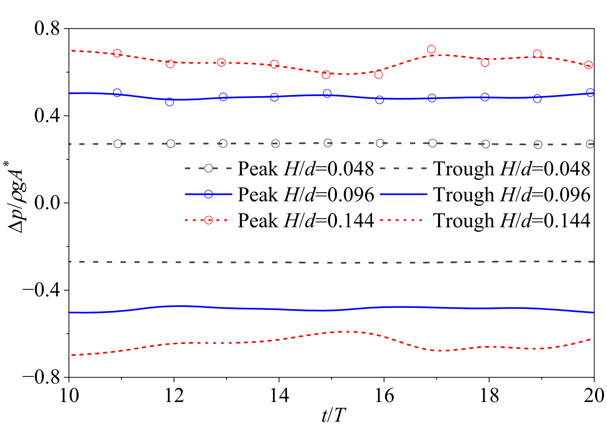

Fig. 25. Time history of wave peak and trough for different wave heights H at kd =1.4, where A^*=0.012 m.

framework can efficiently utilize large-scale parallel computing resources for computationally demanding free-surface wave-structure interaction simulations with satisfactory accuracy shown in Fig. 27.

It should be noted that the comparison in Table 6 is conducted under the same uniform-grid configurations and is not intended to suggest that the present LBM model is generally more efficient than OpenFOAM in all circumstances. OpenFOAM is a mature and stable CFD framework with well-established numerical schemes and support for non-uniform and locally refined meshes, which can significantly improve both accuracy and efficiency in practical engineering simulations. By contrast, the present LBM model is still under development and currently employs a uniform structured grid over the entire computational domain for numerical stability and implementation simplicity. This may introduce unnecessary computational cost in regions where fine resolution is not required, such as the air phase and the tank bottom.

5. Conclusions

A 2D NWT is established using the MRT-LBM to study the hydrodynamic performance of the elastically constrained heave-only OWC WEC. In this model, the VOF method discretized by molecular distribution functions is employed to capture the free surface of water waves, and IBB-GIMEM is extended to address the air-water-solid interactions. Supposing a linear relation between the volume flow rate and pressure drop across PTO system, a pneumatic model is interpolated into this modelling framework to evaluate the power output of the floating WEC. The developed numerical wave model is validated against physical experiments, combining the heave-free box and stationary OWC cases to

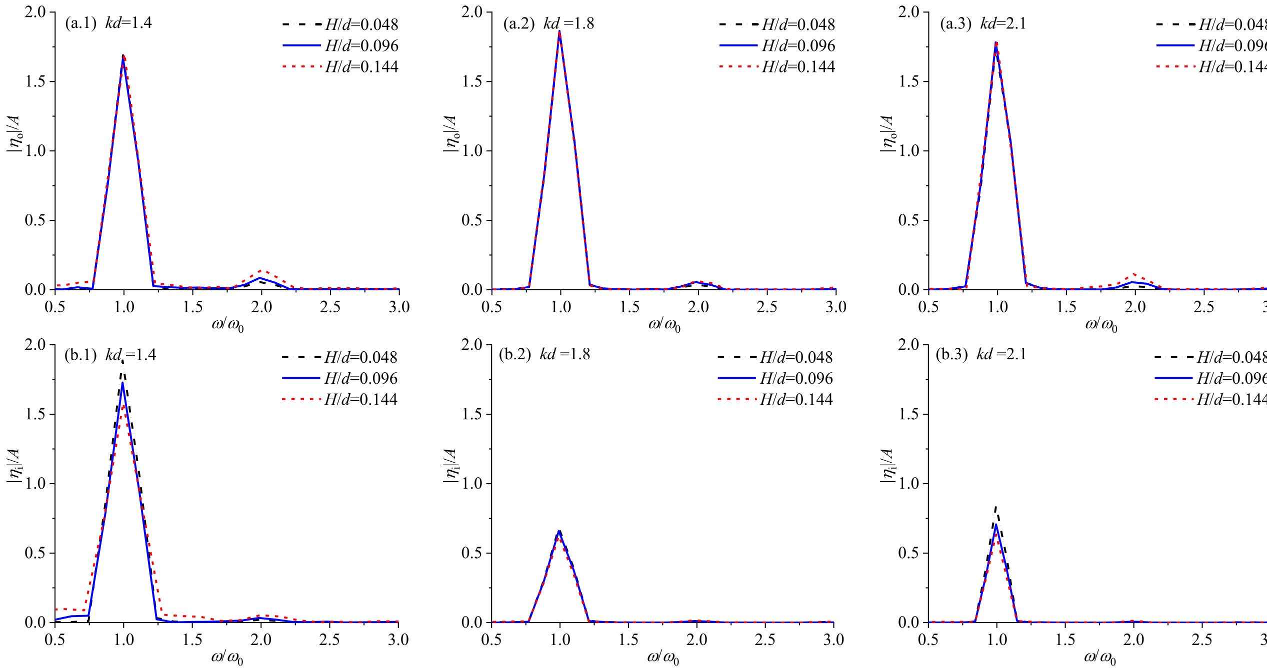

Fig. 26. Amplitude spectra of surface elevation for different wave heights H at kd =1.4, 1.8 and 2.1. (a) Surface elevation η_o at gauge G_o, and (b) surface elevation η_i at gauge G_i.

Table 6
Wall-clock time of OpenFOAM and the present LBM model using different numbers of CPU cores.

Study	Wave propagation (Section 3.1)		Wave-OWC interaction (Section 4) Stationary		Wave-OWC interaction (Section 4) Floating	
	CPU cores	Wall time (s)	CPU cores	Wall time (s)	CPU cores	Wall time (s)
OpenFOAM	128	265,440	128	120,600	-	-
LBM	128	62,720	128	26,470	128	36,350
LBM	512	16,230	256	13,870	256	18,740
LBM	1024	8,647	512	7,682	512	10,500

A uniform grid is adopted over the entire computational domain, and the total number of time steps is fixed at 1.2 million for both cases. Case 1: 4.32 million structured grids (18,000 × 240), time steps 1.66667e-5 s, and spatial resolution 0.001 m. Case 2: 1.89 million structured grids (6300 × 300), time steps 2.88675e-5 s, and spatial resolution 0.0025 m. Note: The OpenFOAM result for the floating OWC case is not reported because its moving-boundary treatment differs from the present LBM model, making a direct comparison not fully consistent, (dynamic or overset meshes vs. simple cut-cell treatment in Cartesian grid).

analyze the capability of prediction on the wave motion and wave-induced heave motion. To reduce computational costs, an efficient theoretical model within a linear potential-flow framework is established and applied prior to the LBM model to identify the most valuable parameters and parameter intervals. The main conclusions of this study are drawn as follows:

(1) The linear potential-flow model effectively identifies the optimal turbine damping, optimal spring stiffness, and resonant frequency intervals. LBM, which accounts for viscous and nonlinear effects, provides a more quantitatively reliable prediction of hydrodynamic efficiency. Overall, the developed staged model, which integrates LBM and potential-flow methods, offers an efficient and reliable approach for predicting the wave energy extraction performance of a floating OWC.
(2) The heave-only OWC can be regarded as a mass-damping-stiffness system with two degrees of freedom: the oscillatory fluid motion within the chamber and the heave motion of the floating structure. Consequently, the coupled system exhibits two natural frequencies: one corresponding to the internal water column resonance, and the other to the heave resonance of the floating body. These two resonance modes interact to shape the system's frequency response and energy conversion efficiency.
(3) As the incident wave height increases, turbulence dissipation becomes stronger, and more energy is transferred to second-order wave components. These effects reduce the hydrodynamic efficiency of the OWC system. To mitigate this adverse effect, it is beneficial to appropriately adjust the turbine damping K_t: decreasing K_t within fluid-resonance-dominant frequency range and increasing K_t in heave-resonance-dominant range.

Overall, the proposed two-dimensional CFD framework based on the Lattice Boltzmann method provides an effective tool for analysing the power extraction performance of OWC wave energy converters. The present work demonstrates the capability of the developed model to capture the key hydrodynamic characteristics of the system, while achieving high computational efficiency and excellent parallel scalability.

However, several limitations relevant to practical engineering applications should be acknowledged. First, the simulations are restricted to two dimensions and therefore cannot fully represent the inherently three-dimensional wave field, spatial flow structures, and geometric effects associated with realistic 3D OWC devices. To address this limitation, we have recently developed a three-dimensional LBM model for a floating cylindrical OWC. In this extension, several key challenges have been tackled, including the evaluation of the interpolation distance q in the IBB treatment, the implementation of the VOF scheme within the D3Q27 lattice framework, and the substantially increased computational cost. Second, the present model adopts a single-phase treatment, which neglects the detailed air-phase dynamics and may limit the accuracy of wave-air-structure interactions under strongly nonlinear conditions. Third, the elastic constraint is represented in a simplified spring-like form, which does not yet reflect the complexity of realistic

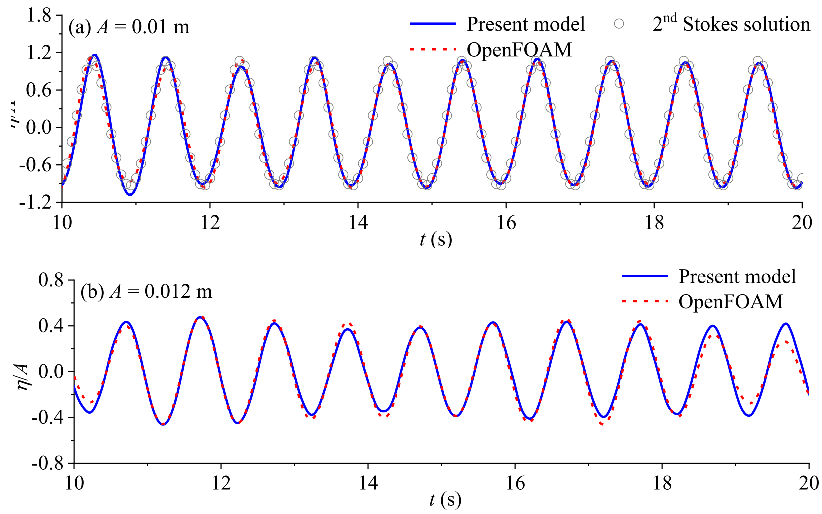

Fig. 27. (a) Water surface displacement of case 1 ($A = 0.01$ m, $T = 1$ s), (b)Water surface displacement at the chamber center of case 2 (stationary OWC, $A = 0.012$ m, $T = 0.99$ s).

mooring tensions. These aspects will be considered in future work to further improve the physical realism and engineering applicability of the proposed framework.

CRediT authorship contribution statement

Baoming Guo: Writing – original draft, Validation, Methodology, Formal analysis. **Dezhi Ning:** Writing – review & editing, Methodology, Conceptualization. **Jianping Meng:** Writing – review & editing, Supervision, Software. **Qianze Zhuang:** Data curation, Formal analysis, Investigation. **Zhihua Xie:** Writing – review & editing, Supervision, Methodology. **Shunqi Pan:** Writing – review & editing, Supervision, Methodology.

Declaration of competing interest

The authors declare that they have no known competing financial interests or personal relationships that could have appeared to influence the work reported in this paper.

Acknowledgements

Support from the UK Engineering and Physical Sciences Research Council under the project "UK Consortium on Mesoscale Engineering Sciences (UKCOMES)" (Grant No. EP/X035875/1) and Wave Energy project (Grant No. EP/V040235/1) is gratefully acknowledged. This work made use of computational support by CoSeC, the Computational Science Centre for Research Communities, through UKCOMES. This work has also been supported by Cardiff University Scholarship and China Scholarship Council (202006060048).

Appendix. Theoretical model

Those velocity potentials can be expressed in each subdomain (I, II, III, IV, and V) shown in Fig. 4 as,

$$\phi_n^{\mathrm{I}} = -\frac{\mathrm{i}gA}{\omega}\sum_{m=0}^{\infty} A_{n,m}^{\mathrm{I}} e^{\lambda_m x}\frac{\cos[\lambda_m(y+d)]}{\cos(\lambda_m d)} - \frac{\mathrm{i}gA}{\omega}\frac{\cosh[k(y+d)]}{\cosh(kd)}e^{\mathrm{i}kx}\delta_{n,0} \tag{A.1}$$

$$\phi_n^{\mathrm{II}} = -\frac{\mathrm{i}gA}{\omega}\left[\begin{array}{c} \left(A_{n,0}^{\mathrm{II}} + B_{n,0}^{\mathrm{II}}x\right)\dfrac{\sqrt{2}}{2} + \\ \displaystyle\sum_{m=1}^{\infty}\left(A_{n,m}^{\mathrm{II}} e^{\gamma_m x} + B_{n,m}^{\mathrm{II}} e^{-\gamma_m x}\right)\cos[\gamma_m(y+d)] \end{array}\right] + \phi_{\mathrm{P}} \tag{A.2}$$

$$\phi_n^{\mathrm{III}} = -\frac{\mathrm{i}gA}{\omega}\sum_{m=0}^{\infty}\left(A_{n,m}^{\mathrm{III}} e^{\lambda_m x} + B_{n,m}^{\mathrm{III}} e^{-\lambda_m x}\right)\frac{\cos[\lambda_m(y+d)]}{\cos(\lambda_m d)} - \frac{\mathrm{i}}{\rho\omega}\delta_{n,2} \tag{A.3}$$

$$\phi_n^{\mathrm{IV}} = -\frac{\mathrm{i}gA}{\omega}\left[\begin{array}{c} \left(A_{n,0}^{\mathrm{IV}} + B_{n,0}^{\mathrm{IV}}x\right)\dfrac{\sqrt{2}}{2} + \\ \displaystyle\sum_{m=1}^{\infty}\left(A_{n,m}^{\mathrm{IV}} e^{\gamma_m x} + B_{n,m}^{\mathrm{IV}} e^{-\gamma_m x}\right)\cos[\gamma_m(y+d)] \end{array}\right] + \phi_{\mathrm{P}} \tag{A.4}$$

$$\phi_n^{\mathrm{V}} = -\frac{\mathrm{i}gA}{\omega}\sum_{m=0}^{\infty} A_{n,m}^{\mathrm{V}} e^{-\lambda_m x}\frac{\cos[\lambda_m(y+d)]}{\cos(\lambda_m d)} \tag{A.5}$$

where λ_m and γ_m are eigenvalues, $A^l_{n,m}$ and $B^l_{n,m}$ is the unknown coefficient is each subdomain (l = I, II, III, IV, V). A is the wave amplitude. ϕ_P are special solutions of velocity potentials in these subdomains II and IV, which can be derived as according to nonhomogeneous boundary conditions,

$$\phi_P = -i\omega\left[\frac{(y+d)^2 - x^2}{2(d-D)}\delta_{n,2} - \frac{(y+d)^2(x-x_0) - (x-x_0)^3/3}{2(d-D)}\delta_{n,3}\right] \tag{A.6}$$

where rotational centre $\boldsymbol{X}_0 = (x_0, y_0)$.

In linear potential-flow model, the energy conservation relation is expressed as follows:

$$K = K_T^2 + K_R^2 + \xi \equiv 1 \tag{A.7}$$

That is to say, the incident wave energy flux equals to the sum of transmission, reflection, and captured energy fluxes. K_T, K_R, and ξ denote the transmission coefficient, reflection coefficient, and hydrodynamic efficiency, respectively.

The numerical results of the total energy flux coefficient K and hydrodynamic efficiency ξ are displayed in Fig. A1 for a heave-only OWC WEC. It can be observed that K equals to 1 for each case at different wave frequency and chamber width. Also, the maximum hydrodynamic efficiency equals to 0.5 for such a symmetric structure, which follows the theoretical derivation by Falnes and Kurniawan (2002). These results validate the present theoretical model.

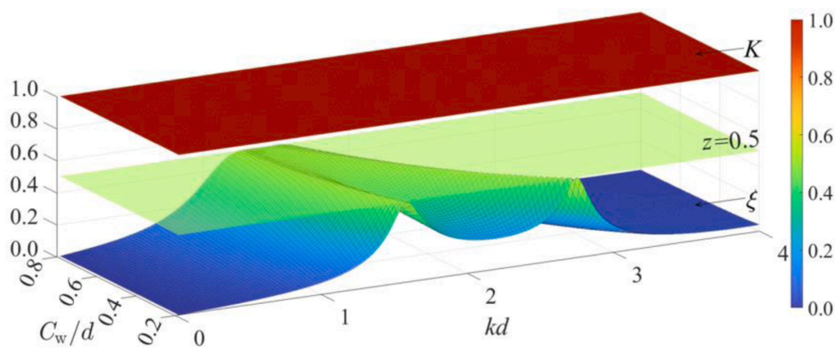

Fig. A1. The total energy coefficient K and hydrodynamic efficiency ξ as functions of wave frequency and chamber width. $d = 0.5$ m, C_w =0.2 m, C_h =0.378 m, B = 0.1 m, $C = 0.1$ m, and $D = 0.252$ m.

References

Choi, J., Yoon, S.B., 2009. Numerical simulations using momentum source wave-maker applied to RANS equation model. Coast. Eng. 56, 1043–1060.

Crespo, A.J.C., Altomare, C., Domínguez, J.M., et al., 2017. Towards simulating floating offshore oscillating water column converters with smoothed particle hydrodynamics. Coast. Eng. 126, 11–26.

Doyle, S., Aggidis, G.A., 2019. Development of multi-oscillating water columns as wave energy converters. Renew. Sustain. Energy Rev. 107, 75–86.

Elhanafi, A., Macfarlane, G., Fleming, A., et al., 2017. Experimental and numerical investigations on the hydrodynamic performance of a floating–moored oscillating water column wave energy converter. Appl. Energy 205, 369–390.

Falcão, A.F.O., Henriques, J.C.C., 2016. Oscillating-water-column wave energy converters and air turbines: a review. Renew. Energy 85, 1391–1424.

Falnes, J., Kurniawan, A., 2002. Ocean Waves and Oscillating Systems. Cambridge University Press.

Ferziger, J.H., PeriC, M. Computational methods for fluid dynamics. 2002.

Fu, L., Cheng, Y., 2023. Hydrodynamic performance of A dual-floater integrated system combining hybrid WECs and floating breakwaters. China Ocean Eng. 36, 969–979.

Gang, A., Guo, B.M., Hu, Z.B., et al., 2022. Performance analysis of a coast - OWC wave energy converter integrated system. Appl. Energy 311.

Guo, B.M., Meng, J.P., Ning, D.Z., et al., 2025a. A Lattice Boltzmann method for free surface flows over partially submerged structures. Comput. Phys. Commun. 317.

Guo, B.M., Meng, J.P., Ning, D.Z., et al., 2025b. An interpolated bounce-back based lattice Boltzmann method for floating structures interacting with free surface flows. J. Comput. Phys. 540.

Guo, B.M., Ning, D.Z., Meng, J.P., et al., 2025c. Non-axisymmetric oscillating water column wave energy converter: a semi-analytical study. Phys. Fluids 37.

Guo, B.M., Ning, D.Z., Wang, R.Q., et al., 2021. Hydrodynamics of an oscillating water column WEC - Breakwater integrated system with a pitching front-wall. Renew. Energy 176, 67–80.

Guo, B.M., Wang, R.Q., Ning, D.Z., et al., 2020. Hydrodynamic performance of a novel WEC-breakwater integrated system consisting of triple dual-freedom pontoons. Energy 209.

Higuera, P., Lara, J.L., Losada, I.J., 2013. Realistic wave generation and active wave absorption for Navier–Stokes models. Coast. Eng. 71, 102–118.

Hu, Z.Z., Greaves, D., Raby, A., 2016. Numerical wave tank study of extreme waves and wave-structure interaction using OpenFoam®. Ocean Eng. 126, 329–342.

Isaacson, M., Baldwin, J., Bhat, S., 1998. Wave propagation past a pile-restrained floating breakwater. Int. J. Offshore Polar Eng. 8, 265–269.

Iturrioz, A., Guanche, R., Lara, J.L., et al., 2015. Validation of OpenFOAM® for oscillating Water column three-dimensional modeling. Ocean Eng. 107, 222–236.

Josset, C., Clément, A.H., 2007. A time-domain numerical simulator for oscillating water column wave power plants. Renew. Energy 32, 1379–1402.

Korner, C., Thies, M., Hofmann, T., et al., 2005. Lattice Boltzmann model for free surface flow for modeling foaming. J. Stat. Phys. 121, 179–196.

Krüger, T., Kusumaatmaja, H., Kuzmin, A., et al., 2017. The Lattice Boltzmann Method. Springer, Cham.

Lallemand, P., Luo, L.S., 2000. Theory of the lattice Boltzmann method: dispersion, dissipation, isotropy, Galilean invariance, and stability. Phys. Rev. E. 61, 6546–6562.

Liu, G., Zhang, J., Zhang, Q., 2021. A high-performance three-dimensional lattice Boltzmann solver for water waves with free surface capturing. Coast. Eng. 165.

Liu, G., Zhang, Q., Zhang, J., 2019a. Numerical wave simulation using a modified lattice Boltzmann scheme. Comput. Fluids 184, 153–164.

Liu, G.-W., Zhang, Q.-H., Zhang, J.-F., 2019b. Development of two-dimensional numerical wave tank based on lattice Boltzmann method. J. Hydrodyn. 32, 116–125.

Liu, X., Lin, P., Shao, S., 2015. ISPH wave simulation by using an internal wave maker. Coast. Eng. 95, 160–170.

Lovas, S., Mei, C.C., Liu, Y., 2010. Oscillating water column at a coastal corner for wave power extraction. Appl. Ocean Res. 32, 267–283.

Luo, Y., Nader, J.-R., Cooper, P., et al., 2014a. Nonlinear 2D analysis of the efficiency of fixed oscillating water column wave energy converters. Renew. Energy 64, 255–265.

Luo, Y., Wang, Z., Peng, G., et al., 2014b. Numerical simulation of a heave-only floating OWC (oscillating water column) device. Energy 76, 799–806.

Martins-rivas, H., Mei, C.C., 2009a. Wave power extraction from an oscillating water column along a straight coast. Ocean Eng. 36, 426–433.

Martins-rivas, H., Mei, C.C., 2009b. Wave power extraction from an oscillating water column at the tip of a breakwater. J. Fluid. Mech. 626, 395–414.

Meng, J., Zhang, Y., Hadjiconstantinou, N.G., et al., 2013. Lattice ellipsoidal statistical BGK model for thermal non-equilibrium flows. J. Fluid. Mech. 718, 347–370.

Mia, M.R., Zhao, M., Wu, H., 2023. Effects of heave motion of an elastically supported floating oscillating water column device on wave energy harvesting efficiency. Phys. Fluids 35.

Najafi-Yazdi, A., Mongeau, L., 2012. An absorbing boundary condition for the Lattice Boltzmann method based on the perfectly matched layer. Comput. Fluids 68, 203–218.

Ning, D.Z., Zhao, X.L., Göteman, M., et al., 2016. Hydrodynamic performance of a pile-restrained WEC-type floating breakwater: an experimental study. Renew. Energy 95, 531–541.

Opoku, F., Uddin, M.N., Atkinson, M., 2023. A review of computational methods for studying oscillating water columns – the Navier-Stokes based equation approach. Renew. Sustain. Energy Rev. 174.

Portillo, J.C.C., Collins, K.M., Gomes, R.P.F., et al., 2020. Wave energy converter physical model design and testing: the case of floating oscillating-water-columns. Appl. Energy 278.

Shan, X., Yuan, X.-F., Chen, H., 2006. Kinetic theory representation of hydrodynamics: a way beyond the Navier–Stokes equation. J. Fluid. Mech. 550.

Simonetti, I., Cappietti, L., El Safti, H., et al., 2015. Numerical modelling of fixed oscillating water column wave energy conversion devices: toward geometry hydraulic optimization. In: International Conference on Ocean, Offshore, and Arctic Engineering (OMAE). Newfoundland, Canada.

Simonetti, I., Cappietti, L., Elsafti, H., et al., 2018. Evaluation of air compressibility effects on the performance of fixed OWC wave energy converters using CFD modelling. Renew. Energy 119, 741–753.

Stoll, S.J.B., 2014. Lattice Boltzmann Simulation of Acoustic fields, With Special Attention to Non-Reflecting Boundary Conditions. Norwegian University of Science and Technology.

Vyzikas, T., Deshoulières, S., Giroux, O., et al., 2017. Numerical study of fixed oscillating Water Column with RANS-type two-phase CFD model. Renew. Energy 102, 294–305.

Wang, C., Xu, H., Zhang, Y., et al., 2023. Hydrodynamic investigation on a three-unit oscillating water column array system deployed under different coastal scenarios. Coast. Eng. 184.

Wang, C., Zhang, Y., Deng, Z., 2022a. Hydrodynamic performance of a heaving oscillating water column device restrained by a spring-damper system. Renew. Energy 187, 331–346.

Wang, C., Zheng, S.M., Zhang, Y.L., 2022b. A heaving system with two separated oscillating water column units for wave energy conversion. Phys. Fluids 34.

Wang, R., Ning, D., Zhang, C., et al., 2018. Nonlinear and viscous effects on the hydrodynamic performance of a fixed OWC wave energy converter. Coast. Eng. 131, 42–50.

Wen, H., Ren, B., Dong, P., et al., 2016. A SPH numerical wave basin for modeling wave-structure interactions. Appl. Ocean Res. 59, 366–377.

Xiao, Y.C., Chu, X.S., Yang, G.W., 2024. Advances of the in-house developed SWLBM framework in simulating large-scale three-dimensional violent free surface flow with intense splashing. Ocean Eng. 309.

Zhang, Y.F., Pan, J.P., Song, M.X., et al., 2025. A multi-phase SPH model for simulating the floating OWC-breakwater integrated systems. Coast. Eng. 197.

Zhao, M., Ning, D., 2024. A review of numerical methods for studying hydrodynamic performance of oscillating water column (OWC) devices. Renew. Energy 233.

Zheng, S., Antonini, A., Zhang, Y., et al., 2019. Wave power extraction from multiple oscillating water columns along a straight coast. J. Fluid. Mech. 878, 445–480.

Zheng, S., Antonini, A., Zhang, Y., et al., 2020. Hydrodynamic performance of a multi-oscillating Water Column (OWC) platform. Appl. Ocean Res. 99.

Zhou, Y., Ning, D., Chen, L., et al., 2023. Experimental investigation on an OWC wave energy converter integrated into a floating offshore wind turbine. Energy Convers. Manag. 276.

Zhu, G.X., Hughes, J., Zheng, S.M., et al., 2023. A novel MPI-based parallel smoothed particle hydrodynamics framework with dynamic load balancing for free surface flow. Comput. Phys. Commun. 284.

Zhuang, Q.Z., Ning, D.Z., Mayon, R., et al., 2024. Experimental and numerical investigation of a land-fixed breakwater-type wave energy converter: an OWC device and a porous plate. Coast. Eng. 194.